

Magneto-optical Kerr effect and signature of the chiral anomaly in a Weyl semimetal in magnetic field

Jean-Michel Parent , René Côté , and Ion Garate

Département de physique and Institut Quantique, Université de Sherbrooke, Sherbrooke, Québec, Canada J1K 2R1



(Received 11 August 2020; accepted 2 December 2020; published 17 December 2020)

One striking property of the Landau level spectrum of a Weyl semimetal (WSM) is the existence of a chiral Landau level, in which the electrons propagate unidirectionally along the magnetic field. This linearly dispersive level influences the optical properties of WSMs. For example, it was recently shown that a complete optical valley polarization is achievable in a time-reversal symmetric Weyl semimetal placed in a magnetic field [S. Bertrand *et al.*, *Phys. Rev. B* **100**, 075107 (2019)]. This effect originates from inter-Landau level transitions involving the chiral Landau level and requires a tilt of the Weyl cones. In this paper we show how the magneto-optical Kerr effect (MOKE) is modified in a WSM with tilted Weyl cones in comparison with its behavior in a normal metal and how a valley polarization can be detected using MOKE. We study both the Faraday (longitudinal) and Voigt (transverse) configurations for light incident on a semi-infinite WSM surface with no Fermi arcs. We use a minimal model of a WSM with four tilted Weyl nodes related by mirror and time-reversal symmetry. In the Voigt configuration, a large peak of the Kerr angle occurs at the plasmon frequency. We show that the blueshift in frequency of this peak with increasing magnetic field is a signature of the chiral anomaly in the MOKE.

DOI: [10.1103/PhysRevB.102.245126](https://doi.org/10.1103/PhysRevB.102.245126)

I. INTRODUCTION

A Weyl semimetal [1] is a three-dimensional topological phase of matter, where pairs of nondegenerate bands cross at isolated points in the Brillouin zone. Near these points, called “Weyl nodes,” the electronic dispersion is gapless and linear in momentum and the excitations satisfy the Weyl equation, a two-component analog of the Dirac equation. Each Weyl node is a source or sink of Berry curvature, which acts as a magnetic field in momentum space, and has a chirality index $\chi = \pm 1$ reflecting the topological nature of the band structure. The Nielsen-Ninomiya theorem [2] requires that the number of Weyl points in the Brillouin zone be even so that Weyl nodes must occur in pairs of opposite chirality. For the Weyl nodes to be stable, either inversion symmetry or time-reversal symmetry must be broken.

Weyl semimetals show a number of interesting transport properties, such as an anomalous Hall effect [3], a chiral-magnetic effect [4], Fermi arcs [5], and a chiral anomaly leading to a negative longitudinal magnetoresistance [6]. The topological aspects of WSMs also show up in their optical properties, especially so when a magnetic field is present. In this case, the linear dispersion is split into positive ($n > 0$) and negative ($n < 0$) energy dispersive Landau levels. The $n = 0$ Landau level is chiral because its dispersion is unidirectional, e.g., $E(k_z) = -\chi v_F k_z$, for a magnetic field along the z direction. The absorption spectrum is different from that of Schrödinger or Dirac fermions [7] and can be used to show the phenomenon of charge pumping due to the chiral anomaly [8] or other photoinduced responses, as well as to distinguish between type I and type II WSMs [9].

In this paper we investigate another optical property that is affected by the topological nature of WSMs, i.e., the magneto-

optical Kerr effect (MOKE), which consists of the rotation of the plane of polarization of a beam of light reflected from the surface of a WSM in a magnetic field. In graphene, also a material with Dirac-like dispersion, a substantial rotation of the polarization plane (> 0.1 rad) upon transmission (the related Faraday effect) has been reported recently [10]. In WSMs, Faraday and Kerr rotations have been studied in some detail in Ref. [11] for a minimal model of a WSM with intrinsically broken time-reversal symmetry (TRS) and no magnetic field. In such a model, the axion term of the electromagnetic action makes a gyrotropic contribution to the dielectric function, thereby leading to Faraday and Kerr rotations in the absence of an external magnetic field.

In the present work our model of a WSM preserves TRS and the Kerr rotation is due to the presence of an external magnetic field, which we set either along the direction of propagation of the incoming electromagnetic wave (i.e., the longitudinal or Faraday configuration) or perpendicular to it (the transverse or Voigt configuration). One motivation for this work is our previous study of the optical absorption [12,13] in WSMs, which predicted the possibility of a complete optical valley polarization for a sizable interval of frequency in a time-reversal symmetric type I WSM with tilted Dirac cones, by a suitable choice of the relative orientation of the incoming light wave, magnetic field, and tilt vector. By complete valley polarization, we mean that two different nodes start absorbing light at a different frequency. This is a property of the electronic structure of the WSM in a magnetic field. The valley polarization shows up as a splitting of the absorption line of two nodes related by TRS at zero magnetic field, for transitions involving the chiral Landau level.

There have been some previous works on the MOKE in WSMs. A giant polarization rotation has been predicted

in type I and type II WSM with tilted cones and broken TRS in zero magnetic field [14]. Kerr and Faraday rotations for zero tilt but finite magnetic field and broken TRS have also been studied [15]. Moreover, experimental evidences for chiral pumping of the Weyl nodes in the WSM TaAs have appeared recently [16,17]. The work we present here is different. We study the MOKE in a simplified model of a WSM with four nodes related by TRS and mirror symmetry in a quantizing magnetic field and in both the Faraday and Voigt geometries. We show that, in contrast with a “normal” metal, in a WSM a sizable Kerr rotation can be expected in both geometries for moderate values of the background dielectric constant ε_∞ . In the resonant regime, where the frequency of the incoming light matches an electronic interband (i.e., inter-Landau level) transition, Kerr rotation can be used as a spectroscopic tool to detect the inter-Landau level transitions. The presence of tilted cones modifies the Landau level quantization and changes the selection rules, giving a much richer interband spectrum in MOKE: when a magnetic field is applied in a direction other than the tilt, interband transitions other than the usual dipolar ones ($|n\rangle \rightarrow |n| \pm 1$) become possible [9]. Moreover, the valley polarization effect we reported earlier for optical absorption also appears in the Kerr rotation, thus providing another way to detect this effect experimentally.

We find that the Voigt configuration is particularly interesting because it enables having a component of the incoming electric field in the direction of the quantizing magnetic field. A consequence of the chiral anomaly in WSMs is that the plasmon frequency ω_p , which is given by the condition that $\text{Re}[\varepsilon_{\parallel}(\omega_p)] = 0$, increases with magnetic field. Here ε_{\parallel} is the element of the dielectric tensor in the direction of the external magnetic field, e.g., ε_{xx} for \mathbf{B} along $\hat{\mathbf{x}}$. In contrast with the Faraday configuration, ε_{\parallel} enters in the definition of the Kerr angle so that we expect that the behavior of the Kerr angle will be modified by the chiral anomaly. Indeed, we show that a strong maximum in the Kerr angle occurs at the plasmon frequency, which is in the THz range for moderate values of ε_∞ , i.e., close to the threshold of the electronic interband transitions. The frequency of this peak increases with magnetic field, providing a clear signature of the chiral anomaly in the Kerr rotation.

The remainder of this paper is organized as follows: Section II introduces our minimal four-node model of a WSM with TRS and tilted cones, and gives the energy spectrum of each node. Section III explains how we compute the dynamical conductivity tensor for both inter- and intra-Landau level transitions. In Sec. IV we give the formalism to compute the Kerr angle in both the Faraday and Voigt configurations. Section V contains our numerical results, which are further summarized in Sec. VI. In order to lighten the main text, we have put details of all calculations in Appendix A for the energy spectrum and Appendix B for the derivation of the current operator for tilted cones. In Appendix C we discuss the MOKE for a normal metal in order to provide a basis for comparison with our findings for a WSM. In Appendix D we derive the magnetic-field dependence of the low-energy peak in the Kerr rotation angle that appears in the Faraday configuration.

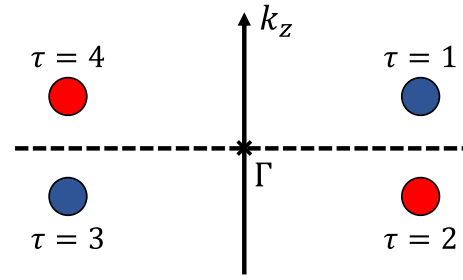


FIG. 1. Toy model of a WSM with time-reversal symmetry and a mirror plane perpendicular to the $\hat{\mathbf{z}}$ direction. The y axis passes through the cross. Blue and red circles indicate Weyl nodes with opposite chiralities.

II. MODEL HAMILTONIAN

We consider a simple model of a WSM, which possesses TRS in the absence of a magnetic field. This toy model has been described and justified in Refs. [12,13], where we used it to calculate the optical valley polarization in a WSM. The model consists of four tilted Weyl nodes (denoted by the index $\tau = 1, 2, 3, 4$), two for each chirality, and a mirror plane placed perpendicularly to the z axis as shown in Fig. 1. Pairs of nodes of opposite chirality ($\tau = 1, 2$ and $\tau = 3, 4$) are related to one another by the mirror plane, while nodes $\tau = 1, 3$ and $\tau = 2, 4$ are related by time-reversal symmetry in the absence of the magnetic field. Thus, the four nodes are symmetry equivalent in the absence of a magnetic field.

The low-energy noninteracting single-particle Hamiltonian for an electron in node $\tau = 1$ is given by

$$h_\tau(\mathbf{p}) = v_F \mathbf{t} \cdot \mathbf{p} \sigma_0 + v_F \mathbf{p} \cdot \boldsymbol{\sigma}, \quad (1)$$

where \mathbf{p} is the momentum of the electron measured with respect to the Weyl node, $\boldsymbol{\sigma}$ is a vector of Pauli matrices in the $1/2$ -pseudospin state of the two bands at their crossing points, σ_0 is the 2×2 unit matrix, v_F is the Fermi velocity, and \mathbf{t} is a dimensionless vector describing the magnitude and direction of the tilt of the Weyl cone. We restrict our analysis to a type I WSM, i.e., to $|\mathbf{t}| < 1$. The Hamiltonians of the other three Weyl nodes are obtained by applying mirror and time-reversal operations to $h_1(\mathbf{p})$. These amount to making the transformations

$$\begin{aligned} \tau = 1 \rightarrow 2 : (v_F, t_x, t_y, t_z) &\rightarrow (-v_F, -t_x, -t_y, t_z), \\ \tau = 1 \rightarrow 3 : (v_F, t_x, t_y, t_z) &\rightarrow (v_F, -t_x, -t_y, -t_z), \\ \tau = 1 \rightarrow 4 : (v_F, t_x, t_y, t_z) &\rightarrow (-v_F, t_x, t_y, -t_z), \end{aligned} \quad (2)$$

where we have assumed that $\boldsymbol{\sigma}$ transforms as a spin under time-reversal and mirror operations (see Ref. [13] for a discussion of this point).

A transverse static magnetic field \mathbf{B}_0 is added via the Peierls substitution $\mathbf{p} \rightarrow \mathbf{P} = \mathbf{p} + e\mathbf{A}$. While it is possible to obtain the energy levels of the Hamiltonian analytically [9], we find it more convenient to use a numerical approach in order to get a fully orthonormal basis for the eigenspinors. Moreover, a numerical approach allows a study of the system for arbitrary orientations of the magnetic field and tilt vector. It also allows the consideration of more

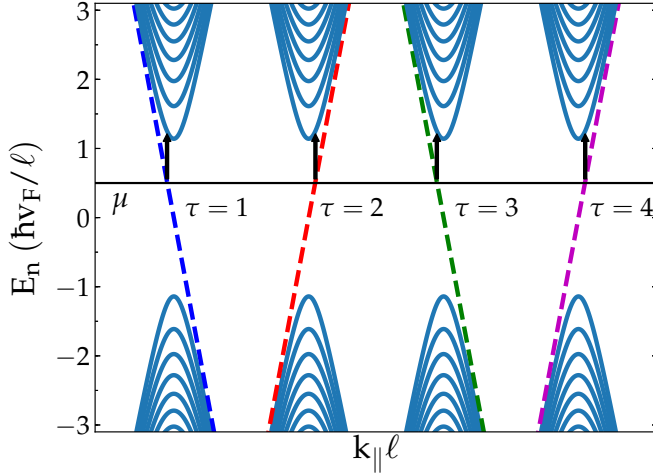


FIG. 2. Dispersion of the first Landau levels of the four nodes for $\mathbf{t} = t\hat{z}$ and $\mathbf{B} = B_0\hat{x}$. The chiral Landau level is represented by the dashed line. The length of each arrow indicates the lowest-energy interband transition under right circularly polarized light. When the tilt vectors of the nodes are perpendicular to the static magnetic field, all nodes have the same interband absorption threshold. For clarity, the position of the different nodes has been shifted in $k_{\parallel}\ell$.

complex Hamiltonians with, for example, nonlinear terms in the energy spectrum [13]. The numerical diagonalization of $h_1(\mathbf{P})$ is carried out in Appendix A. The many-body Hamiltonian in the basis of the Landau levels of $h_1(\mathbf{P})$ can be written as

$$\mathcal{H} = \sum_{\tau, X, p_{\parallel}, I} E_I(\tau, p_{\parallel}) d_I^{\dagger}(\tau, X, p_{\parallel}) d_I(\tau, X, p_{\parallel}). \quad (3)$$

In Eq. (3) the eigenstates are defined by the set of quantum numbers $(I, X, p_{\parallel}, \tau)$, where X is the guiding-center index and $I = (n, s)$ is the Landau level index. Our convention is to take $n = 0, 1, 2, 3, \dots$ as a positive number and use $s = +1$ (-1) for the positive (negative)-energy levels. The variable $p_{\parallel} = \hbar k_{\parallel}$ is the momentum in the direction of the magnetic field, which we set along the z (or x) axis, i.e., perpendicular (or parallel) to the mirror plane. Each Landau level (I, p_{\parallel}, τ) has the macroscopic degeneracy $N_{\varphi} = S/2\pi\ell^2$, where $\ell = \sqrt{\hbar/eB_0}$ is the magnetic length and S is the area of the WSM perpendicular to the magnetic field. The operator $d_I^{\dagger}(\tau, X, p_{\parallel})$ creates an electron in the quantum state $(I, p_{\parallel}, X, \tau)$.

The dispersion of the Landau levels is given in Figs. 2 and 3 for $\mathbf{t} \perp \mathbf{B}$ and $\mathbf{t} \parallel \mathbf{B}$, respectively. The arrows in these figures indicate the energy gap for interband transitions when the Fermi level E_F is in the chiral Landau level (i.e., $n = 0$). The optical gaps are identical for all nodes when the tilt and magnetic field are perpendicular to each other. When the magnetic field is perpendicular to the mirror plane and has a nonzero projection along the tilt vector, the optical gaps for interband transitions involving the chiral Landau level are different for nodes that are related by time-reversal symmetry when $\mathbf{B}_0 = 0$, but equal for nodes that are mirror partners (see Ref. [12] for a discussion on general orientations of \mathbf{B}). When light propagates along the direction of the magnetic

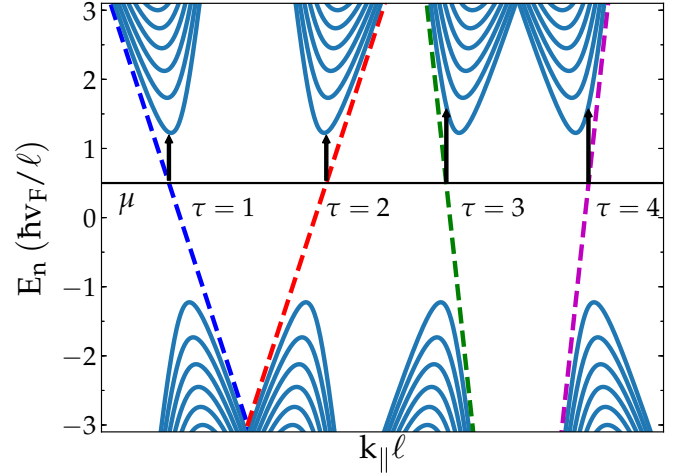


FIG. 3. Dispersion of the Landau levels for the four nodes for $\mathbf{t} = t\hat{z}$ and $\mathbf{B} = B_0\hat{z}$. The chiral Landau level is represented by the dashed line. The length of each arrow indicates the lowest-energy interband transition under right circularly polarized light. When the tilt vectors of the nodes have nonzero components along the static magnetic field, different pairs of nodes have different interband absorption thresholds in the quantum limit, thereby leading to a valley polarization. For clarity, the position of the different nodes has been shifted in $k_{\parallel}\ell$.

field, this difference in the absorption gap leads to a full valley polarization [12].

III. OPTICAL CONDUCTIVITY

The magneto-optical conductivity of Weyl semimetals has been calculated before [18]. The effect of a tilt on the AC optical response has also been considered in a model of a WSM with broken TRS and no quantizing magnetic field [19]. Here we consider the effect of a tilt on the four-node model introduced above (which has TRS) and in the presence of a quantizing magnetic field. We restrict ourselves to $T = 0$ K. Since we are mainly interested in the behavior of the Kerr angle in the resonant regime, i.e., in the THz range of frequencies, finite temperature effects should be negligible for experiments carried out at low temperature, i.e., at a few Kelvin.

The single-particle current operator for node τ is defined by

$$\mathbf{j}_{\tau} = - \left. \frac{\partial h_{\tau}(\mathbf{p})}{\partial \mathbf{A}_{\text{ext}}} \right|_{\mathbf{A}_{\text{ext}} \rightarrow 0} = -e v_F (\boldsymbol{\sigma} + \mathbf{t} \sigma_0), \quad (4)$$

where \mathbf{A}_{ext} is the vector potential of an external electromagnetic field. The many-body current is

$$\begin{aligned} \mathbf{J}_{\tau} &= \int d^3r \psi_{\tau}^{\dagger}(\mathbf{r}) \mathbf{j}_{\tau} \psi_{\tau}(\mathbf{r}) \\ &= -e v_F \sum_{\tau, p_{\parallel}, X} \sum_{I, J} \Upsilon_{I, J}(\tau, p_{\parallel}) d_I^{\dagger}(\tau, X, p_{\parallel}) d_J(\tau, X, p_{\parallel}), \end{aligned} \quad (5)$$

where the matrix elements $\Upsilon_{I, J}(\tau, p_{\parallel})$ are given in Eq. (B4) of Appendix B.

It is convenient to define the operator

$$\rho_{I,J}(\tau, p_{\parallel}) = \frac{1}{N_{\varphi}} \sum_X d_I^{\dagger}(\tau, X, p_{\parallel}) d_J(\tau, X, p_{\parallel}), \quad (6)$$

so that the many-body Hamiltonian and current can be written as

$$\mathcal{H} = \sum_{\tau, p_{\parallel}, I} E_I(\tau, p_{\parallel}) \rho_{I,I}(\tau, p_{\parallel}) \quad (7)$$

and

$$\mathbf{J}_{\tau} = -ev_F \sum_{p_{\parallel}} \sum_{I,J} \Upsilon_{I,J}(\tau, p_{\parallel}) \rho_{I,J}(\tau, p_{\parallel}). \quad (8)$$

The optical conductivity tensor is related to the retarded current response function $\chi_{\alpha,\beta}^R(\omega) = \chi_{\alpha,\beta}^R(\mathbf{q} = 0, \omega)$ by

$$\sigma_{\alpha,\beta}(\omega) = \frac{i}{\omega} [\chi_{\alpha,\beta}^R(\omega) - \chi_{\alpha,\beta}^R(0) \delta_{\alpha\beta}], \quad (9)$$

where $\alpha, \beta \in \{x, y, z\}$ and ω is the frequency of the incoming light beam. The diamagnetic contribution to the current operator is lacking in the continuum approximation of the linear spectrum of the low-energy model. This absence leads to unphysical terms [11] in $\sigma_{\alpha,\beta}(\omega)$. The second term on the right-hand side of Eq. (9) is required in order to remove these spurious contributions.

The retarded current response function can be obtained from the two-particle Matsubara Green's function

$$\begin{aligned} \chi_{\alpha,\beta}(\tau) &= -\frac{1}{\hbar V} \langle T_{\tau} J_{\alpha}(\tau) J_{\beta}(0) \rangle \\ &= -e^2 v_F^2 \frac{1}{\hbar V} \sum_{I,J} \sum_{K,L} \sum_{p_{\parallel}, p'_{\parallel}} \Upsilon_{I,J}^{(\alpha)}(p_{\parallel}) \Upsilon_{K,L}^{(\beta)}(p'_{\parallel}) \\ &\quad \times \langle T_{\tau} \rho_{I,J}(\tau, p_{\parallel}) \rho_{K,L}(0, p'_{\parallel}) \rangle, \end{aligned} \quad (10)$$

where T_{τ} is the time ordering operator and τ an imaginary time, not to be confused with the node index. We omit the node index in the remaining of this section in order to avoid any confusion. In linear response, $\chi_{\alpha,\beta}(\tau)$ is approximated by

$$\begin{aligned} \chi_{\alpha,\beta}(\tau) &= e^2 v_F^2 \frac{1}{\hbar V} \sum_{I,J} \sum_{X, p_{\parallel}} \Upsilon_{I,J}^{(\alpha)}(p_{\parallel}) \Upsilon_{J,I}^{(\beta)}(p_{\parallel}) \\ &\quad \times G_{I,X}(p_{\parallel}, -\tau) G_{J,X}(p_{\parallel}, \tau), \end{aligned} \quad (11)$$

where the single-particle Matsubara Green's function is defined by

$$G_{I,X}(p_{\parallel}, \tau) = -\langle T_{\tau} d_I(p_{\parallel}, \tau) d_I^{\dagger}(p_{\parallel}, 0) \rangle. \quad (12)$$

Fourier-transforming $\chi_{\alpha,\beta}(\tau)$, we get the familiar result, for each node,

$$\begin{aligned} \chi_{\alpha,\beta}(i\Omega_p) &= \int_0^{\beta\hbar} d\tau e^{i\Omega_p \tau} \chi_{\alpha,\beta}(\tau) \\ &= \frac{e^2 v_F^2}{\beta \hbar^2 V} \sum_{\omega_n} \sum_{I,J} \sum_{X, p_{\parallel}} \Upsilon_{I,J}^{(\alpha)}(p_{\parallel}) \Upsilon_{J,I}^{(\beta)}(p_{\parallel}) \\ &\quad \times G_{I,X}(p_{\parallel}, i\omega_n) G_{J,X}(p_{\parallel}, i\Omega_p + i\omega_n), \end{aligned} \quad (13)$$

where Ω_p, ω_n are, respectively, bosonic and fermionic Matsubara frequencies. The current-current response has contributions from both intra- and inter-Landau level transitions. We

compute them separately in the following sections. Moreover, the total current response and the related dielectric tensor are obtained by summing the individual current response of the four nodes.

The fact that the total optical conductivity is given by the sum of node-resolved optical conductivities is a consequence of the vanishing of the interband matrix elements of the current operator between states that are located in different Weyl nodes. At first glance, the vanishing of the matrix element is not obvious in the presence of a magnetic field. For example, when the magnetic field is pointing along the z direction, the energy spectra of nodes 1 and 2 as a function of k_z will be superposed with the energy spectra of nodes 4 and 3, respectively. Yet, it turns out that the interband transitions induced by light do not mix the states originating from different nodes.

The underlying reason for this may be easily understood in the Landau gauge, where two components of the crystal momentum remain good quantum numbers. One of the components is the momentum along the magnetic field, while the other component is perpendicular to it (and is often disguised in the form of the guiding center). The translational symmetry along this second direction is key to ensure that interband transitions induced by light do not mix different nodes.

For example, suppose that we take the magnetic field along the z direction. Nodes 1 and 4 in Fig. 1 have the same k_z coordinate, but a vastly different k_x coordinate. Choosing the Landau gauge such that k_x is a good quantum number, it follows from translational symmetry that light (whose wave vector is essentially zero compared to the separation of the nodes in k_x) cannot connect bands from node 1 with bands from node 4. A similar argument can be employed for other orientations of the magnetic field.

On a related note, if the magnetic length becomes comparable to or shorter than the inverse of the distance in momentum space that separates two Weyl nodes at zero field, then a hybridization takes place between those two nodes and gaps open in the chiral Landau levels. In that regime, if the Fermi level falls inside the gap, chirality is not a good quantum number even at low energy, and our theory no longer applies. Yet, significant hybridization effects have been reported only at ultrahigh magnetic fields [20].

A. Inter-Landau-level contributions to the current response function $\chi_{\alpha,\beta}(\omega)$

With the Hamiltonian given by Eq. (3), the single-particle Matsubara Green's function is simply

$$G_{I,X}(p_{\parallel}, i\omega_n) = \frac{1}{i\omega_n - [E_I(p_{\parallel}) - \mu]/\hbar}, \quad (14)$$

where μ is the chemical potential. It is independent of the guiding-center index X .

Performing the frequency sum in Eq. (13) and taking the analytic continuation $i\Omega_p \rightarrow \omega + i\delta$, we get for each node τ the interband response function

$$\begin{aligned} \chi_{\alpha,\beta}^R(\omega) &= -\frac{e^2 v_F^2}{4\pi^2 \ell^2 \hbar^2} \sum_{\substack{I,J \\ (I \neq J)}} \int dp_{\parallel} \Upsilon_{I,J}^{(\alpha)}(p_{\parallel}) \Upsilon_{J,I}^{(\beta)}(p_{\parallel}) \\ &\quad \times \frac{f[E_J(p_{\parallel})] - f[E_I(p_{\parallel})]}{\omega + i\delta - [E_J(p_{\parallel}) - E_I(p_{\parallel})]/\hbar}, \end{aligned} \quad (15)$$

where $f(E) = 1/(e^{\beta(E-\mu)} + 1)$ is the Fermi function, $\beta = 1/k_B T$, and k_B is the Boltzmann constant. At $T = 0$ K, $\mu \rightarrow E_F$ and $f[E_J(p_{\parallel})] \rightarrow \Theta[E_F - E_J(p_{\parallel})]$, where $\Theta(x)$ is the step function and E_F is the Fermi level. Only transitions between an occupied and an unoccupied level can contribute to the response function.

In Eq. (15) the effects of disorder and finite resolution of the measurement apparatus have been included phenomenologically via a small broadening parameter $\delta \simeq 0.05$ meV. This broadening does not have a significant effect in our main results, provided that the inter-Landau level spacing near the Fermi level is large compared to δ . Such is the case for us.

B. Intra-Landau-level contribution to the response function $\chi_{\alpha,\beta}(\omega)$

We consider the situation where the Fermi level lies in the chiral level $n = 0$, above $E = 0$ but below the energy of the level $n = 1$. The only allowed intra-Landau level transitions are then those that take place in the chiral level. To calculate their contribution to the current response function, disorder needs to be considered. The spectral representation of the disorder-averaged single-particle Green's function in level $n = 0$ is given by

$$\langle G_{0,X}(p_{\parallel}, i\omega_n) \rangle = \int_{-\infty}^{+\infty} d\omega \frac{A_0(p_{\parallel}, \omega)}{i\omega_n - \omega}, \quad (16)$$

with the spectral weight approximated by the Lorentzian shape

$$A_0(p_{\parallel}, \omega) = \frac{\Gamma/\pi}{\{\omega - [E_0(p_{\parallel}) - \mu]/\hbar\}^2 + \Gamma^2}, \quad (17)$$

where $\Gamma = 1/2\tau_0$, with τ_0 the momentum relaxation time. The current response function becomes

$$\begin{aligned} \chi_{\alpha,\beta}(i\Omega_p) &= \frac{e^2 v_F^2 N_{\varphi}}{\hbar V} \sum_{p_{\parallel}} \Upsilon_{0,0}^{(\alpha)}(p_{\parallel}) \Upsilon_{0,0}^{(\beta)}(p_{\parallel}) \\ &\times \frac{1}{\beta \hbar} \sum_{\omega_n} \int_{-\infty}^{+\infty} d\omega' \frac{A_0(p_{\parallel}, \omega')}{i\Omega_p + i\omega_n - \omega'} \\ &\times \int_{-\infty}^{+\infty} d\omega'' \frac{A_0(p_{\parallel}, \omega'')}{i\omega_n - \omega''}. \end{aligned} \quad (18)$$

Performing the Matsubara frequency sum and taking the analytical continuation $i\Omega_p \rightarrow \omega + i\delta$, we get

$$\begin{aligned} \chi_{\alpha,\beta}^R(\omega) &= \frac{e^2 v_F^2}{2\pi \ell^2 \hbar^2} \int \frac{dp_{\parallel}}{2\pi} \Upsilon_{0,0}^{(\alpha)}(p_{\parallel}) \Upsilon_{0,0}^{(\beta)}(p_{\parallel}) \\ &\times \int_{-\infty}^{+\infty} d\omega' \int_{-\infty}^{+\infty} d\omega'' a_0(p_{\parallel}, \omega') \\ &\times a_0(p_{\parallel}, \omega'') \frac{f(\omega'') - f(\omega')}{\omega + i\delta + \omega'' - \omega'}, \end{aligned} \quad (19)$$

where we have defined

$$a_0(p_{\parallel}, \omega) = A_0(p_{\parallel}, \omega + \mu/\hbar). \quad (20)$$

Defining also

$$g_0(p_{\parallel}, \omega) = \frac{\omega - E_0(p_{\parallel})/\hbar}{[\omega - E_0(p_{\parallel})/\hbar]^2 + \Gamma^2}, \quad (21)$$

we get, at zero temperature and after some simple algebra,

$$\begin{aligned} \chi_{\alpha,\beta}^R(\omega) &= \frac{e^2 v_F^2}{2\pi \ell^2 \hbar^2} \int \frac{dp_{\parallel}}{2\pi} \Upsilon_{0,0}^{(\alpha)}(p_{\parallel}) \Upsilon_{0,0}^{(\beta)}(p_{\parallel}) \\ &\times \left[\int_{-\infty}^{+E_F/\hbar} d\omega' a_0(p_{\parallel}, \omega') \right. \\ &\times [g_0(p_{\parallel}, \omega' + \omega) + g_0(p_{\parallel}, \omega' - \omega)] \\ &\left. - i\pi \int_{E_F/\hbar - \omega}^{E_F/\hbar} d\omega' a_0(p_{\parallel}, \omega') a_0(p_{\parallel}, \omega' + \omega) \right]. \end{aligned} \quad (22)$$

Thus, the intraband conductivity in the chiral level is given by

$$\begin{aligned} \sigma_{\alpha,\beta}^{\text{intra}}(\omega) &= \frac{e^2 v_F^2}{2\pi \ell^2 \hbar^2} \frac{i}{\omega} \int \frac{dp_{\parallel}}{2\pi} \Upsilon_{0,0}^{(\alpha)}(p_{\parallel}) \Upsilon_{0,0}^{(\beta)}(p_{\parallel}) \\ &\times \left[\int_{-\infty}^{+E_F/\hbar} d\omega' a_0(p_{\parallel}, \omega') K(p_{\parallel}, \omega, \omega') \right. \\ &\left. - i\pi \int_{E_F/\hbar - \omega}^{E_F/\hbar} d\omega' a_0(p_{\parallel}, \omega') a_0(p_{\parallel}, \omega' + \omega) \right], \end{aligned} \quad (23)$$

with the function

$$\begin{aligned} K(p_{\parallel}, \omega, \omega') &= g_0(p_{\parallel}, \omega' + \omega) + g_0(p_{\parallel}, \omega' - \omega) \\ &- 2\delta_{\alpha,\beta} g_0(p_{\parallel}, \omega'). \end{aligned} \quad (24)$$

In the absence of a tilt, only the matrix element $\Upsilon_{0,0}^{(\alpha)}(p_{\parallel})$ for α in the direction of the magnetic field is nonzero. Thus, only the conductivity $\sigma_{\parallel}(\omega)$ [which is $\sigma_{xx}(\omega)$ for $\mathbf{B} = B_0 \hat{\mathbf{x}}$ and $\sigma_{zz}(\omega)$ for $\mathbf{B} = B_0 \hat{\mathbf{z}}$] is nonzero. From Eq. (23) we get (for each node)

$$\text{Re}[\sigma_{\parallel}(\omega)] = \frac{v_F e^3 \tau_0}{4\pi^2 \hbar^2} \frac{B_0}{1 + (\omega\tau_0)^2}, \quad (25)$$

$$\text{Im}[\sigma_{\parallel}(\omega)] = \omega\tau_0 \text{Re}[\sigma_{\parallel}(\omega)]. \quad (26)$$

Our results for the conductivity contain the momentum instead of the transport relaxation time since vertex corrections are not included in our calculation of the current response function. Yet, in the quantum limit, only internode scattering leads to the relaxation of the charge current. Hence, below we will associate τ_0 with the internode scattering time.

A finite tilt modifies the matrix elements $\Upsilon_{0,0}^{(\alpha)}(p_{\parallel})$ and makes the other elements of the conductivity tensor nonzero, in particular $\sigma_{\perp}(\omega)$ [i.e., $\sigma_{zz}(\omega)$ for $\mathbf{B} = B_0 \hat{\mathbf{x}}$ and $\sigma_{xx}(\omega)$ for $\mathbf{B} = B_0 \hat{\mathbf{z}}$], which enters in the definition of the Kerr angle for the Voigt configuration, as we show below.

With τ_0 and v_F independent of the magnetic field, Eq. (25) shows that the conductivity $\text{Re}[\sigma_{\parallel}(\omega)]$ increases linearly with the magnetic field. This negative magnetoresistance is a signature of the chiral anomaly in Weyl semimetals [6], where collinear electric and magnetic fields ($\mathbf{E} \cdot \mathbf{B} \neq 0$) result in a transport of electrons between two Weyl nodes of opposite chirality. It is known, however, that τ_0 varies with magnetic field in a way that depends on the type of disorder considered. For instance, in the case of short-ranged neutral impurities, $\text{Re}[\sigma_{\parallel}(\omega)]$ becomes independent of B . The B dependence of v_F can further alter the sign of the magnetoresistance [21,22].

As a result, the B dependence of $\text{Re}[\sigma_{\parallel}(\omega)]$ is not robustly linked to the chiral anomaly.

In contrast, the situation appears to be more promising when it comes to the plasmon frequency ω_p . At $q = 0$, ω_p is given by the condition

$$\text{Re}[\varepsilon_{\parallel}(\omega_p)] = 0, \quad (27)$$

i.e.,

$$1 - \frac{\text{Im}[\sigma_{\parallel}(\omega_p)]}{\varepsilon_0 \omega_p} = 0, \quad (28)$$

which gives

$$1 - \frac{1}{\varepsilon_0} \frac{v_F e^3}{4\pi^2 \hbar^2} \frac{\tau_0^2}{1 + (\omega_p \tau_0)^2} B_0 = 0. \quad (29)$$

The plasmon frequency occurs at high frequency (in the THz range in WSMs), which can exceed the momentum scattering rate. When $\omega_p \tau_0 \gg 1$, one has, adding the contributions of the four nodes,

$$\omega_p^2 = 4 \frac{e^2 v_F}{4\pi^2 \hbar^2 \varepsilon_0} = 4 \frac{e^3 v_F B_0}{4\pi^2 \hbar^2 \varepsilon_0}, \quad (30)$$

where ε_0 is the permittivity of free space (in general to be multiplied by ε_{∞} due to screening from high-energy electronic bands). The linear increase with magnetic field of ω_p^2 is also a signature of the chiral anomaly [6] and should not be modified by disorder insofar as $\omega_p \tau_0 \gg 1$. This trend remains likewise robust to the B dependence of v_F (neglected herein). In a normal metal, the plasmon frequency $\omega_{p,\text{metal}}^2 = n_e e^2 / m \varepsilon_0$, with n_e the electronic density and m the effective mass of the electron, is independent of the magnetic field (see Appendix C). The dispersion relation of the plasmon mode in WSMs and normal metals are discussed in more detail in Ref. [23]. The plasmon frequency, or equivalently the zero of the longitudinal dielectric function, increases as $\sqrt{B_0}$. When interband transitions are considered, ω_p is shifted to a lower frequency as shown in Fig. 4, although it remains in the THz range.

In the derivation of Eq. (30), we have neglected the tilt of the Weyl cones. Simple analytical considerations show that, in our model, the component of the tilt parallel to the magnetic field does not change Eq. (30). The component of the tilt perpendicular to the magnetic field is more complicated to treat analytically; we have established numerically that it shifts the plasmon frequency to lower frequencies [relative to that expected from Eq. (30)], without altering the field dependence of the plasmon frequency qualitatively.

In the derivation of Eq. (30), we have likewise neglected the band curvature of the chiral Landau levels. This curvature becomes significant as we approach the energy scale where two different chiral Landau levels connect with one another. In order to investigate the influence of band curvature in the plasmon frequency, we consider a spin-degenerate tight-binding dispersion $\varepsilon_k = -2\gamma \cos(ka)$, for which the long-wavelength density response function in the quantum limit reads

$$\chi_{n,n}^R(q, \omega) \approx \frac{4N_{\varphi}}{\pi \hbar^2 S} \frac{1}{a\omega^2} \gamma (qa)^2 \sin(k_F a), \quad (31)$$

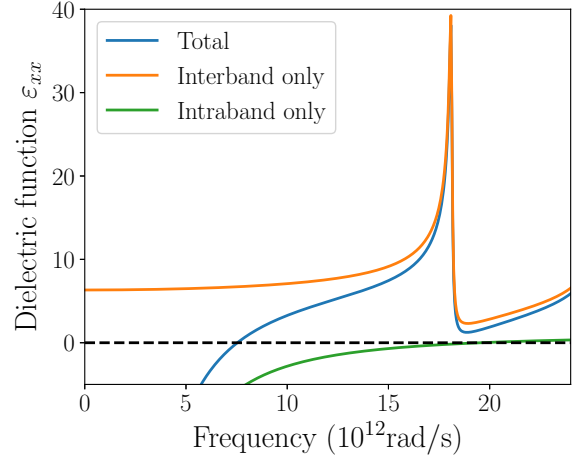


FIG. 4. Real part of the relative dielectric function $\varepsilon_{\parallel} = \varepsilon_{xx}$ as a function of ω for an external static magnetic field $\mathbf{B} = B_0 \hat{\mathbf{x}}$ with $B_0 = 0.3$ T. The zero of $\varepsilon_{\parallel}(\omega)$, which gives the plasmon frequency, is pushed to a lower frequency when inter-Landau level contributions are considered. Parameters: Total electronic density $n_e = 1 \times 10^{20} \text{ m}^{-3}$, momentum relaxation time $\tau_0 = 10$ ps, Fermi velocity $v_F = 3 \times 10^5$ m/s, and tilt $t = 0$.

where a is the lattice constant, $k_F = n_e \pi^2 \ell^2$ is the Fermi momentum, n_e is the electron density, and $v_F = 2\gamma a \sin(k_F a) / \hbar$ is the Fermi velocity. It follows that

$$\omega_p^2 = \frac{e^2}{\pi^2 \ell^2 \hbar \varepsilon_0} \frac{2\gamma a}{\hbar} \sin(k_F a) = \frac{e^2 v_F}{\pi^2 \ell^2 \hbar \varepsilon_0}. \quad (32)$$

In the low-density limit ($n_e \ell^2 a \ll 1$), when the Fermi level is close to the bottom of the dispersion, the plasmon frequency is independent of the magnetic field and given by

$$\omega_p^2 = \frac{e^2}{\varepsilon_0} \frac{1}{\hbar^2} 2\gamma a^2 n_e. \quad (33)$$

This is the result expected for a parabolic band dispersion with an effective mass $\hbar^2 / (2\gamma a^2)$. At higher densities, when the Fermi level lies close to the region where the dispersion is linear, such that $\sin(k_F a) \simeq 1$, we recover Eq. (30). Thus, we learn that Eq. (30) holds in the quantum limit provided that the Fermi level lies in the regime where the energy dispersion is linear; such is the case in the Weyl semimetals of interest.

IV. FORMALISM FOR THE MAGNETO-OPTICAL KERR EFFECT

We consider an electromagnetic wave arriving at normal incidence on a surface of a semi-infinite WSM that has no Fermi arcs. The Maxwell equations in regions 1 (the vacuum) and 2 (the WSM) are

$$\nabla \cdot \mathbf{D} = \rho_f; \quad \nabla \times \mathbf{E} = -\frac{\partial \mathbf{B}}{\partial t}, \quad (34)$$

$$\nabla \cdot \mathbf{B} = 0; \quad \nabla \times \mathbf{H} = \mathbf{j}_f + \frac{\partial \mathbf{D}}{\partial t}, \quad (35)$$

where ρ_f and \mathbf{j}_f are the free charge and current densities. We assume that the WSM is nonmagnetic so that $\mathbf{B} = \mu_0 \mathbf{H}$ with μ_0 the permeability of free space. We use the constitutive

relation $\mathbf{D} = \epsilon_0 \overleftrightarrow{\epsilon} \cdot \mathbf{E}$, where $\overleftrightarrow{\epsilon}$ is the *relative* dielectric tensor which is related to the conductivity tensor $\overleftrightarrow{\sigma}$ by

$$\overleftrightarrow{\epsilon} = \overleftrightarrow{\mathbf{I}} + i \frac{\overleftrightarrow{\sigma}}{\epsilon_0 \omega}, \quad (36)$$

with $\overleftrightarrow{\mathbf{I}}$ the unit tensor and ϵ_0 the permittivity of free space. To account for the high-energy transitions not included in our calculation, the unit tensor $\overleftrightarrow{\mathbf{I}}$ should be replaced by the relative dielectric tensor $\overleftrightarrow{\epsilon}_\infty$ whose precise form depends on the particular WSM considered. In our calculation we take $\overleftrightarrow{\epsilon}_\infty = \epsilon_\infty \overleftrightarrow{\mathbf{I}}$ with $\epsilon_\infty = 1$. Because ϵ_∞ can be quite big in WSMs, we discuss the effects of increasing ϵ_∞ on the Kerr angle in Sec. VI.

From the Maxwell equations, the dispersion relation of an electromagnetic wave in both regions (with $\overleftrightarrow{\epsilon} = \overleftrightarrow{\mathbf{I}}$ in region 1) is given by

$$q^2 \mathbf{E} - (\mathbf{q} \cdot \mathbf{E}) \mathbf{q} = \frac{\omega^2}{c^2} \overleftrightarrow{\epsilon} \cdot \mathbf{E}. \quad (37)$$

At the interface between vacuum and WSM, the electromagnetic field must obey the boundary conditions

$$\begin{aligned} (\mathbf{D}_1 - \mathbf{D}_2) \cdot \hat{\mathbf{n}} &= \sigma_f, & (\mathbf{B}_1 - \mathbf{B}_2) \cdot \hat{\mathbf{n}} &= 0, \\ \mathbf{E}_1^\parallel - \mathbf{E}_2^\parallel &= 0, & \mathbf{H}_1^\parallel - \mathbf{H}_2^\parallel &= 0, \end{aligned} \quad (38)$$

where $\hat{\mathbf{n}}$ is a vector normal to the WSM surface, pointing from region 2 to 1. \mathbf{E}_i^\parallel , \mathbf{H}_i^\parallel (with $i = 1, 2$) are the field components parallel to the surface of the WSM, which we take to be the x - y plane at $z = 0$.

The incident wave is assumed to be linearly polarized in the x - y plane: $\mathbf{E}_I(z, t) = (E_0^x \hat{\mathbf{x}} + E_0^y \hat{\mathbf{y}}) e^{i(qz - \omega t)}$. Its dispersion relation is $q^2 = \omega^2/c^2$, where c is the speed of light in vacuum. The reflected wave is given by

$$\begin{aligned} \mathbf{E}_R(z, t) &= [(r_{xx} E_0^x + r_{xy} E_0^y) \hat{\mathbf{x}} \\ &+ (r_{yx} E_0^x + r_{yy} E_0^y) \hat{\mathbf{y}}] e^{-i(qz + \omega t)}, \end{aligned} \quad (39)$$

where r_{ij} are complex reflection coefficients that depend on the orientation of the magnetic field, tilt vector, and mirror plane. We consider two different cases in the following sections: the longitudinal and transverse configurations.

A. Longitudinal propagation ($\mathbf{q} \parallel \mathbf{B}_0 \parallel \hat{\mathbf{z}}$)

In the longitudinal configuration, the electromagnetic wave propagates in the direction of the external magnetic field. If the external magnetic field \mathbf{B}_0 and the tilt vector \mathbf{t} are in the $\hat{\mathbf{z}}$ direction, perpendicular to the mirror plane, then the total dielectric tensor (sum of the four nodes) has the form

$$\overleftrightarrow{\epsilon} = \begin{pmatrix} \epsilon_{xx} & \epsilon_{xy} & 0 \\ -\epsilon_{xy} & \epsilon_{xx} & 0 \\ 0 & 0 & \epsilon_{zz} \end{pmatrix}. \quad (40)$$

In this situation, Maxwell equations support in the WSM two elliptically polarized electromagnetic waves, the analog of the right (RCP) and left (LCP) circularly polarized waves, with electric fields $E_+ = E_x + iE_y$ and $E_- = E_x - iE_y$. The transmitted electric fields for these two solutions are

given by

$$\begin{aligned} \mathbf{E}_T^{(\pm)}(z, t) &= [(t_{xx}^{(\pm)} E_0^x + t_{xy}^{(\pm)} E_0^y) \hat{\mathbf{x}} \\ &+ (t_{yx}^{(\pm)} E_0^x + t_{yy}^{(\pm)} E_0^y) \hat{\mathbf{y}}] e^{-i(q_\pm z - \omega t)}, \end{aligned} \quad (41)$$

where $t_{ij}(\omega)$ are complex transmission coefficients. The component $E_{T,z} = 0$ so that the wave is transverse in both media and there is no induced charge (i.e., $\nabla \cdot \mathbf{D} = 0$) in the WSM. The dispersion relations are

$$q_\pm^2(\omega) = \frac{\omega^2}{c^2} (\epsilon_{xx} \pm i\epsilon_{xy}) \equiv \frac{\omega^2}{c^2} \epsilon_\mp(\omega) = q^2 \epsilon_\mp(\omega), \quad (42)$$

with $q = \omega/c$.

The total electric fields in regions 1 and 2 are given by

$$\mathbf{E}_1(z, t) = \mathbf{E}_I(z, t) + \mathbf{E}_R(z, t), \quad (43)$$

$$\mathbf{E}_2(z, t) = \mathbf{E}_T^+(z, t) + \mathbf{E}_T^-(z, t), \quad (44)$$

with the magnetic fields obtained from Faraday's law.

Applying the boundary conditions to the total electric and magnetic field and isolating the reflection coefficients, we get

$$r_{xx}(\omega) = r_{yy}(\omega) = \frac{1 - \sqrt{\epsilon_+ \epsilon_-}}{(1 + \sqrt{\epsilon_+})(1 + \sqrt{\epsilon_-})}, \quad (45a)$$

$$r_{yx}(\omega) = -r_{xy}(\omega) = \frac{i(\sqrt{\epsilon_+} - \sqrt{\epsilon_-})}{(1 + \sqrt{\epsilon_+})(1 + \sqrt{\epsilon_-})}. \quad (45b)$$

In this configuration the incident wave is taken to be linearly polarized at an angle $\theta_I = \pi/4$ from the x axis with amplitude E_0^x along both directions of the x - y plane, so that the reflected electric field is

$$\mathbf{E}_R(z, t) = [E_R^x(\omega) \hat{\mathbf{x}} + E_R^y(\omega) \hat{\mathbf{y}}] e^{-i(qz + \omega t)}, \quad (46)$$

with

$$E_R^x(\omega) = [r_{xx}(\omega) + r_{xy}(\omega)] E_0^x, \quad (47)$$

$$E_R^y(\omega) = [r_{xx}(\omega) - r_{xy}(\omega)] E_0^x. \quad (48)$$

The coefficients $r_{ij}(\omega)$ are obtained from the dielectric tensor $\overleftrightarrow{\epsilon}$, which contains the combined current response function of the four nodes.

B. Transverse propagation ($\mathbf{q} \perp \mathbf{B}_0 \parallel \hat{\mathbf{x}}$)

In the transverse configuration, the electromagnetic wave still propagates along the z axis, but the external magnetic field is taken to point in the direction $\hat{\mathbf{x}}$, i.e., parallel to the mirror plane. For a tilt along the z axis, the dielectric tensor for this configuration has the form

$$\overleftrightarrow{\epsilon} = \begin{pmatrix} \epsilon_{xx} & 0 & 0 \\ 0 & \epsilon_{yy} & \epsilon_{yz} \\ 0 & -\epsilon_{yz} & \epsilon_{zz} \end{pmatrix} \quad (49)$$

when the contributions of the four nodes are taken into account.

Maxwell's equations give again two dispersion relations: one where the electric field \mathbf{E}_\parallel of the incident light is polarized along x , i.e., parallel to the static magnetic field, giving the

dispersion relation

$$q_{\parallel}^2 = \frac{\omega^2}{c^2} \varepsilon_{xx}, \quad (50)$$

and one where the electromagnetic wave is polarized along y , i.e., perpendicular to the static magnetic field with the dispersion relation

$$q_{\perp}^2 = \frac{\omega^2}{c^2} \left(\varepsilon_{yy} + \frac{\varepsilon_{yz}^2}{\varepsilon_{zz}} \right) = \frac{\omega^2}{c^2} \varepsilon_v, \quad (51)$$

where ε_v is called the Voigt dielectric function [24]. In this later case there is an induced field in the direction of propagation, given by

$$E_z = -\frac{\varepsilon_{zy}}{\varepsilon_{zz}} E_y, \quad (52)$$

so that the electric field for this polarization, in medium 2, is given by

$$\mathbf{E}_{\perp} = E_y \left(\hat{\mathbf{y}} - \frac{\varepsilon_{zy}}{\varepsilon_{zz}} \hat{\mathbf{z}} \right). \quad (53)$$

The induced charge is still zero, however. The transmitted wave in the WSM is given by

$$\mathbf{E}_T^{(\pm)}(z, t) = t_{\parallel} \mathbf{E}_{\parallel} e^{-i(q_{\parallel} z - \omega t)} + t_{\perp} \mathbf{E}_{\perp} e^{-i(q_{\perp} z - \omega t)}, \quad (54)$$

where t_{\parallel}, t_{\perp} are the transmission coefficients for the parallel and transverse polarizations. In the Voigt configuration, the polarization vector of an incident electromagnetic wave polarized at an angle with respect to the x axis in the x - y plane will rotate in the WSM because of the different refractive indices for the parallel and transverse polarizations. There is no rotation if the polarization vector is only along the x or y axis. This form of dichroism can also lead to a sizable Kerr rotation as we show in Sec. V. Solving Eqs. (37) and (38) gives the reflected field components

$$\begin{aligned} E_R^x(\omega) &= \frac{1 - \sqrt{\varepsilon_{xx}}}{1 + \sqrt{\varepsilon_{xx}}} E_0^x(\omega), \\ E_R^y(\omega) &= \frac{1 - \sqrt{\varepsilon_v}}{1 + \sqrt{\varepsilon_v}} E_0^y(\omega). \end{aligned} \quad (55)$$

C. Definition of the Kerr angle

We define the phases θ_R^x and θ_R^y by

$$E_R^x = |E_R^x| e^{i\theta_R^x}, \quad E_R^y = |E_R^y| e^{i\theta_R^y}, \quad (56)$$

where $|E_R^i|, \theta_R^i$ (with $i = x, y$) are, respectively, the moduli and associated phases of the complex components of the reflected wave. The reflected electric field at $z = 0$ is then

$$\mathbf{E}(t) = |E_R^x| \cos(\theta_R^x - \omega t) \hat{\mathbf{x}} + |E_R^y| \cos(\theta_R^y - \omega t) \hat{\mathbf{y}}. \quad (57)$$

The polarization of the reflected field is strongly modified as the frequency is varied. It could be linear, elliptical, or circular. The sense of rotation of the polarization can also change with ω . A complete description of the reflected field would give $\mathbf{E}(t)$ over one period of oscillation. Experimentally, however, what is reported is the Kerr angle θ_K and ellipticity ϕ_K defined by

$$\tan(\theta_K + \theta_I) = \left| \frac{E_R^y}{E_R^x} \right|, \quad (58)$$

where θ_I is the polarization angle of the incident linearly polarized wave, and the ellipticity

$$\phi_K = \theta_R^x - \theta_R^y. \quad (59)$$

In the Faraday configuration, with an incident wave linearly polarized at an angle $\theta_I = \pi/4$ with respect to the x axis, the Kerr angle is given by

$$\tan(\theta_K + \theta_I) = \left| \frac{1 + i(\sqrt{\varepsilon_+} - \sqrt{\varepsilon_-}) - \sqrt{\varepsilon_+ \varepsilon_-}}{1 - i(\sqrt{\varepsilon_+} - \sqrt{\varepsilon_-}) - \sqrt{\varepsilon_+ \varepsilon_-}} \right|, \quad (60)$$

while in the Voigt configuration for the identically polarized incident wave, the Kerr angle is

$$\tan(\theta_K + \theta_I) = \left| \frac{(1 - \sqrt{\varepsilon_v})(1 + \sqrt{\varepsilon_{xx}})}{(1 + \sqrt{\varepsilon_v})(1 - \sqrt{\varepsilon_{xx}})} \right|. \quad (61)$$

As mentioned above, Eqs. (60) and (61) do not define precisely (i.e., in the range $[-\pi, \pi]$) the polarization angle of the reflected electric field. Instead, the Kerr angle $\theta_K + \theta_I$ is defined in the range $[0, \pi/2]$. Since we take $\theta_I = \pi/4$ in our calculations, we get a θ_K that can be positive or negative which indicates that the polarization angle increases or decreases from $\pi/4$, giving a peak or a dip (inverted peak) in the curve of $\theta_K(\omega)$.

V. NUMERICAL RESULTS FOR THE KERR ANGLE

We compute the Kerr angle in the four-node model for two specific configurations: (1) the longitudinal Faraday configuration where $\mathbf{q} \parallel \mathbf{B}_0 \parallel \hat{\mathbf{z}}$ and the linear polarization vector is $\hat{\mathbf{e}} \perp \mathbf{B}_0$; and (2) the transverse Voigt configuration where $\mathbf{q} \parallel \hat{\mathbf{z}}$, $\mathbf{B}_0 = B_0 \hat{\mathbf{x}} \perp \mathbf{q}$ and the linear polarization vector $\hat{\mathbf{e}}$ is in the x - y plane. For the Faraday configuration we choose the magnetic field to be perpendicular to the mirror plane while we take it in the mirror plane in the Voigt configuration. Other choices are, of course, possible. We assume a total electronic density of $n_e = 1 \times 10^{20} \text{ m}^{-3}$ for the four nodes. For the interband transitions we introduce the scattering rate phenomenologically by taking a finite but small value of δ in the conductivity tensor. For the intraband transitions, disorder is taken into account explicitly by introducing a Lorentzian broadening $\Gamma = 1/2\tau_0$ with $\tau_0 = 10^{-11} \text{ s}$. In both configurations, the tilt vector is taken to be $\mathbf{t} = t_0 \hat{\mathbf{z}}$ with $t_0 = 0.5$, so that $\mathbf{t} \parallel \mathbf{B}_0$ in the Faraday configuration and $\mathbf{t} \perp \mathbf{B}_0$ in the Voigt configuration. This is done in order to isolate the main features of the Kerr angle in both configurations, i.e., valley polarization in the former, and chiral anomaly in the latter. In the presentation of our results, we change the notation for the Landau level index, i.e., we choose n to be positive for $s = +1$ and negative for $s = -1$. The chiral Landau level is still $n = 0$.

A. Faraday configuration

When the external magnetic field has a nonzero projection along the tilt vector, an optical valley polarization effect appears in the absorption spectrum. This effect results in a splitting of the interband transition peaks $0 \rightarrow |n|$ and $-|n| \rightarrow 0$ that involve the chiral Landau level. One pair of nodes starts absorbing light at a lower frequency than the other pair, leading to a valley polarization. This phenomenon was

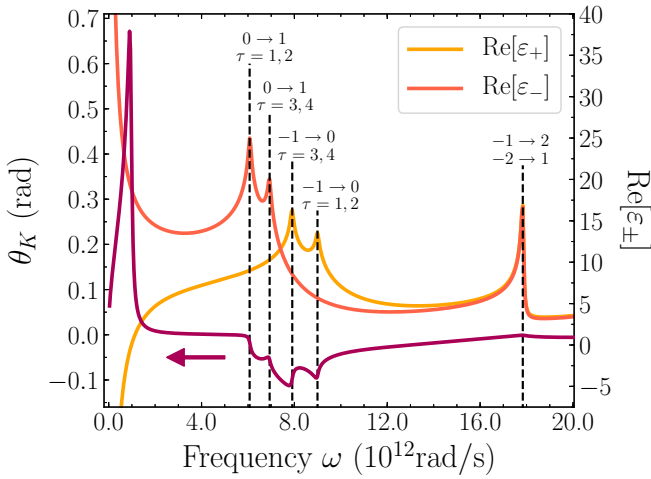


FIG. 5. Frequency dependence of the Kerr angle θ_K and real part of the dielectric functions ε_+ and ε_- in the Faraday configuration, where \mathbf{q} , \mathbf{B}_0 , $\mathbf{t} \parallel \hat{\mathbf{z}}$. The interband transitions contributing to the main peaks are indicated. The $0 \rightarrow 1$ and $-1 \rightarrow 0$ transitions are each split into two as a consequence of valley polarization; the Weyl nodes τ contributing to each of the subpeaks are indicated. Parameters: $B_0 = 0.2$ T, $n_e = 1 \times 10^{20} \text{ m}^{-3}$, $v_F = 3 \times 10^5 \text{ m/s}$, $\mathbf{t} = 0.5\hat{\mathbf{z}}$.

studied extensively in our previous work on the absorption spectrum of a WSM [12]. Here we show that it is also possible to probe it using the MOKE.

A plot of the Kerr angle versus frequency is shown in Fig. 5 for the case where the vectors \mathbf{q} , \mathbf{B}_0 , \mathbf{t} are all parallel to the z axis and so perpendicular to the mirror plane. The incident wave is assumed linearly polarized in the x - y plane with $\theta_I = \pi/4$ and the Fermi level is in the chiral Landau level. In this configuration only the dipolar transitions are permitted. The allowed interband transitions are visible as a succession of dips in the curve of the Kerr angle vs frequency for $\omega \gtrsim 4 \times 10^{12} \text{ rad/s}$ or peaks in the dielectric functions $\text{Re}[\varepsilon_{\pm}(\omega)]$. The curve of $\theta_K(\omega)$ shows a large peak around $\omega \approx 1 \times 10^{12} \text{ rad/s}$, which coincides with the frequency ω_+ where $\text{Re}[\varepsilon_+(\omega)] = 0$. Figure 6 shows that this large peak in $\theta_K(\omega)$ is redshifted in frequency when the magnetic field increases, which is also the behavior of the frequency $\omega_+(B)$. A similar shift happens in a normal metal (see Appendix C). In Appendix D we show that this large peak in $\theta_K(\omega)$ comes mostly from the pair of transitions $n = -1 \rightarrow n = 0$ and $n = 0 \rightarrow n = -1$ and show that the frequency shift is inversely proportional to the magnetic field B_0 . We remark that τ_0 does not enter in the calculation of the Kerr angle, i.e., in Eq. (60), in this configuration.

Figure 5 shows that nodes related by time-reversal symmetry (TRS), i.e., nodes 1 and 3 or 2 and 4, have different optical gaps in the Faraday configuration. This causes a splitting of the dips in $\theta_K(\omega)$ or the peaks in $\text{Re}[\varepsilon_{\pm}(\omega)]$ corresponding to the transitions $0 \rightarrow 1$ and $-1 \rightarrow 0$. (Note that we could have chosen a different Faraday configuration leading to no splitting.) The other interband peaks in $\text{Re}[\varepsilon_{\pm}(\omega)]$, corresponding to transitions between nonchiral Landau levels, are not split. By contrast, when $\mathbf{t} \cdot \mathbf{B}_0 = 0$ for all nodes, transitions $0 \rightarrow 1$ (or $-1 \rightarrow 0$) are equivalent for all four nodes and therefore, only a single dip or peak is present for each

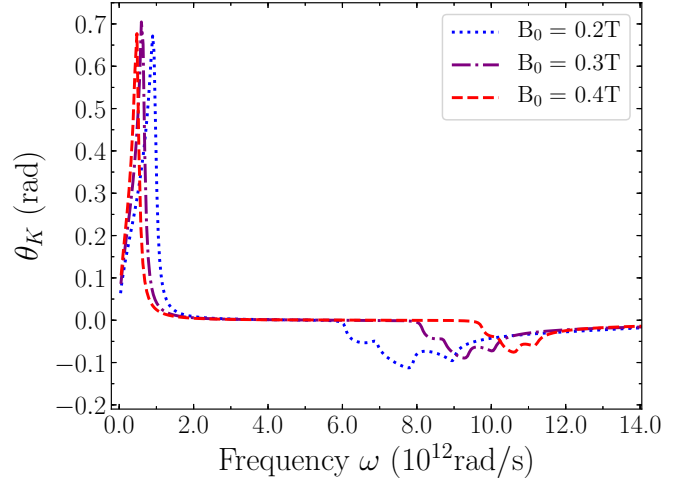


FIG. 6. Kerr angle as a function of frequency for different values of the magnetic field $\mathbf{B} = B_0 \hat{\mathbf{z}}$ in the Faraday configuration. Parameters: $n_e = 1 \times 10^{20} \text{ m}^{-3}$, $v_F = 3 \times 10^5 \text{ m/s}$, $\mathbf{t} = 0.5\hat{\mathbf{z}}$.

transition $0 \rightarrow 1$ or $-1 \rightarrow 0$. With a linearly polarized incident wave, both $0 \rightarrow 1$ and $-1 \rightarrow 0$ transitions are excited. For a circularly polarized light, either the $0 \rightarrow 1$ or $-1 \rightarrow 0$ transition is excited. (More specifically, the transitions $|n| \rightarrow |n| + 1$ show up in ε_- and the transitions $|n| \rightarrow |n| - 1$ in ε_+ , as in graphene.) The valley polarization effect due to a finite tilt, for transitions involving the chiral level, are thus detectable in the Kerr rotation spectra.

Using Eq. (A23), the energy gap between two Landau levels $n, m \neq 0$ of a tilted Weyl cone is independent of the node index and increases with magnetic field. As we just showed, the gap involving the chiral level behaves differently. If the Fermi level is not at the neutrality point, it depends on the node index and the splitting of the $0 \rightarrow 1$ (or $-1 \rightarrow 0$) peak decreases with increasing magnetic field as can be seen in Fig. 6. This behavior is also present in the absorption spectrum (see Fig. 9 of Ref. [12]). It follows that, in the quantum limit, the valley polarization is present in the Kerr rotation angle in a larger range of frequencies as the magnetic field is decreased. The splitting can also be increased by increasing the tilt. It would be interesting to measure these effects experimentally.

B. Voigt configuration

In the Voigt configuration, the magnetic field $\mathbf{B} = B_0 \hat{\mathbf{x}}$ is perpendicular to the propagation vector $\mathbf{q} \parallel \hat{\mathbf{z}}$ and the tilt vector $\mathbf{t} \parallel \hat{\mathbf{z}}$ and the polarization vector $\hat{\mathbf{e}}$ lies in the x - y plane. As Eq. (55) shows, in order to see a Kerr rotation in the Voigt configuration, the polarization of the incident wave propagating along the z direction must make an angle with the x and y axis. We choose $\theta_I = \pi/4$ and $E_0^x = E_0^y = E_0$ for the incoming electric field. Then, the reflected electric field is given by

$$E_R^x(\omega) = \frac{1 - \sqrt{\varepsilon_{xx}}}{1 + \sqrt{\varepsilon_{xx}}} E_0(\omega), \quad E_R^y(\omega) = \frac{1 - \sqrt{\varepsilon_v}}{1 + \sqrt{\varepsilon_v}} E_0(\omega), \quad (62)$$

with $\varepsilon_v = \varepsilon_{yy} + \varepsilon_{yz}^2/\varepsilon_{zz}$.

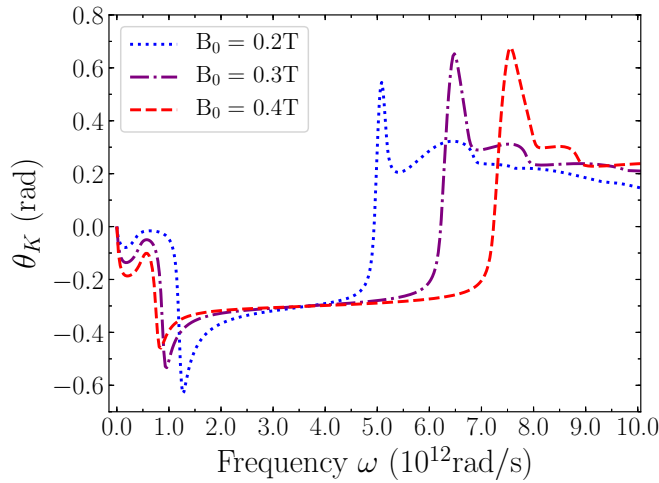


FIG. 7. Kerr angle as a function of frequency for different magnetic fields in the Voigt configuration. The blueshift of the large peak in θ_K is related to the chiral anomaly. Parameters: $n_e = 1 \times 10^{20} \text{ m}^{-3}$, $\tau_0 = 10 \text{ ps}$, $v_F = 3 \times 10^5 \text{ m/s}$, $\mathbf{t} = 0.5\hat{z}$.

We first remark that if interband transitions are not included in the calculation of the dielectric functions, then $\varepsilon_{yy} = 1$ and $\varepsilon_{yz} = 0$ so that $\varepsilon_v = 1$. It then follows from Eq. (62) that $E_R^y(\omega) = 0$, and so $\tan(\theta_K + \theta_I) = 0$, giving $\theta_K = -\pi/4$. There is no structure in the Kerr angle in this case. When both intraband and interband transitions are included, the behavior of the Kerr angle with frequency and magnetic field is shown in Fig. 7. We notice that the Kerr angle in this configuration is as big as in the Faraday configuration, in contrast to a normal metal (where it is at least ten times smaller). Moreover, its behavior is clearly different from that in the Faraday configuration. The strong peak in the Kerr angle at high frequency occurs when $\text{Re}[\varepsilon_{xx}(\omega)] = 0$, i.e., at the WSM plasmon frequency $\omega = \omega_p$ given by Eq. (30), as can be seen in Fig. 8. The peak is also present at zero tilt, and its frequency increases as $\sqrt{B_0}$. In an ordinary metal, the frequency of the peak in the Kerr angle increases proportionally to B_0^2 . Moreover, in a metal, the negative peak in the Kerr angle

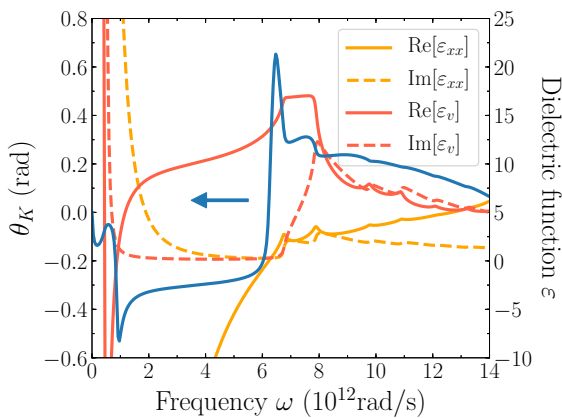


FIG. 8. Frequency dependence of the dielectric functions ε_{xx} and ε_v and of the Kerr angle θ_K for a magnetic field $B = 0.3 \text{ T}$. Parameters: $n_e = 1 \times 10^{20} \text{ m}^{-3}$, $\tau_0 = 10 \text{ ps}$, $v_F = 3 \times 10^5 \text{ m/s}$, $\mathbf{t} = 0.5\hat{z}$. The first four peaks in $\text{Re}[\varepsilon_{xx}]$ come from the transitions: $0 \rightarrow 1$, $-1 \rightarrow 0$, $0 \rightarrow 2$, $-2 \rightarrow 0$.

occurs at the plasmon frequency $\omega_{p,\text{metal}} = \sqrt{ne^2/m\varepsilon_0}$, which is independent of B_0 . In contrast, in a WSM, the negative peak occurs when $\text{Re}[\varepsilon_v(\omega)] = 0$ (see Fig. 8) and is redshifted with magnetic field. In this figure the plasmon frequency is below the interband absorption threshold. This is a common circumstance, especially if we take into account the effect of ε_∞ which reduces the plasmon frequency without changing the optical gap for interband transitions.

The blueshift of the strong peak in the Kerr angle in a WSM is consistent with the measurement by Levy *et al.* (see Fig. 2(d) of Ref. [16]) of the blueshift of the reflectance edge in the Weyl semimetal TaAs. As we pointed out in Sec. III, this magnetoresistance effect is a signature of the chiral anomaly in a WSM and, as Fig. 7 clearly shows, it is reflected in the displacement of the peak in the Kerr angle. This peak is caused mainly by the intraband contribution of the chiral Landau level to the longitudinal conductivity σ_{xx} (i.e., σ_{\parallel}). Since it occurs at the plasmon frequency given in Eq. (30), which is independent of τ_0 in the limit $\omega_p\tau_0 \gg 1$, it is not affected by the magnetic-field dependence of τ_0 . We have checked numerically that taking $\tau_0 \propto 1/B_0$ or $\tau_0 \propto 1/B_0^2$ does not change the position of this peak.

The peak disappears if the intraband part of σ_{xx} is set to zero, but is almost unchanged if σ_{zz} (i.e., σ_{\perp}) is zero. As discussed in Sec. III, the interband transitions produce a redshift of the plasmon frequency. The shift of the Kerr angle occurs in the THz range and should be measurable in optical experiments. The blueshift of the strong peak in the Kerr angle with magnetic field in the Voigt geometry contrasts with its behavior in the Faraday configuration, where it is redshifted with the magnetic field. The Voigt geometry is special because the longitudinal dielectric function (e.g., ε_{xx} when $\mathbf{B}_0 \parallel \hat{\mathbf{x}}$) enters the definition of the Kerr angle, while it does not in the Faraday configuration.

Aside from the large maximum caused by intraband transitions, the Kerr angle displays additional smaller peaks originating from interband transitions. The first four of these peaks, also visible in $\text{Re}[\varepsilon_{xx}(\omega)]$ (see Fig. 8), occur at the transitions $0 \rightarrow 1$; $-1 \rightarrow 0$; $0 \rightarrow 2$ and $-2 \rightarrow 0$. Because we choose $\mathbf{t} \perp \mathbf{B}$ [i.e., $t_{\parallel} = 0$ in Eq. (A23)], there is no splitting of the $0 \rightarrow 1$ and $-1 \rightarrow 0$ peaks and so no valley polarization in the Kerr angle.

Figures 7 and 8 show some intriguing structure in the low-frequency region. However, as this low-frequency behavior will likely be strongly affected by details of the disorder, for example the impact of the B dependence of the scattering time, we will not discuss it further in this paper.

VI. SUMMARY AND DISCUSSION

We have shown that a sizable Kerr rotation is possible in a simplified model of a Weyl semimetal in both the Faraday and Voigt configurations. Inter-Landau level transitions appear as dips or peaks in a plot of the Kerr angle vs frequency and can be detected in this way. Moreover, a tilt of the Weyl cones allows the detection of transitions beyond the dipolar ones. In the particular Faraday configuration that we have chosen to study, with a nonzero tilt of the Weyl cones in the direction of the external magnetic field, the peaks in the Kerr angle that represent interband transitions involving the chiral Landau

level are split into subpeaks. This splitting, which we found before in the absorption spectrum, is a manifestation of a full valley polarization in a WSM [12]. A valley polarization is thus also detectable via the magneto-optical Kerr effect.

We have also demonstrated the interest of measuring the MOKE in the Voigt geometry. In this configuration, the Kerr angle involves the longitudinal dielectric function $\varepsilon_{||}(\omega)$, unlike in the Faraday configuration, since the electric field of the wave has a nonzero projection on the external magnetic field. The zero of the longitudinal dielectric function gives the plasmon frequency ω_p . The chiral anomaly in a WSM leads to an increase of ω_p with the external static magnetic, i.e., $\omega_p \propto \sqrt{B_0}$. In the Voigt geometry, a large peak in the Kerr angle θ_K occurs at ω_p and is consequently blueshifted by a magnetic field. We argued that the $\sqrt{B_0}$ shift of this peak is the signature of the chiral anomaly in the MOKE, just like the shift of the absorption edge recently reported in reflectance measurements [16].

The exact size of the Kerr angle depends, of course, on the dielectric constant ε_∞ , which can be quite large in WSMs. We have verified that using a larger value of ε_∞ in our calculation (instead of $\varepsilon_\infty = 1$) does indeed reduce the amplitude of the Kerr angle signal and redshifts the frequencies of the peaks and dips. For $\varepsilon_\infty = 30$, the amplitude of the peak in θ_K at $B = 0.3$ T in Fig. 7 is decreased from 0.65 to 0.41 rad and ω_p is reduced to $\omega_p \approx 2.5 \times 10^{12}$ rad/s. If ε_∞ is very large, the peak $\theta_K(\omega_p)$ may be blurred by disorder. For the chiral anomaly to be detected in the Kerr angle, the plasmon frequency must satisfy the condition $\omega_p \tau_0 \gg 1$.

We have chosen a total electronic density of $n_e = 1 \times 10^{20} \text{ m}^{-3}$ for our calculation, as we did not have a particular WSM in mind. At such a small density, the quantum limit is reached at a very small value of B_0 , i.e., ≈ 0.053 T. To be certain that this choice does not affect the main conclusions of our paper, and to get a quantum limit closer to recently reported electronic density values [16,25,26], we have recalculated Fig. 7 for a much bigger total density of $n_e = 1 \times 10^{22} \text{ m}^{-3}$ and a magnetic field of $B_0 = 7.83$ T (the value of B_0 needed to obtain the same Fermi level as in Fig. 7 for $B_0 = 0.3$ T). The qualitative aspects of the curve remain unchanged, with almost the same amplitude for the peaks and dips, but with the peak at $\theta_K(\omega_p)$ now shifted to $\approx 32 \times 10^{12}$ rad/s, i.e., ≈ 21 meV. Thus, an increase in the carrier density could compensate for the redshift created by a larger value of ε_∞ .

Although our calculations have been carried out for a toy model, the main predictions derived from them are qualitatively applicable to real WSMs. For example, let us consider TaAs, which displays two symmetry-inequivalent multiplets of Weyl nodes (8 W1 nodes and 16 W2 nodes).

Two simple observations can be made at strong enough magnetic fields, when the quantum limit is attained for both W1 and W2 nodes. On the one hand, if \mathbf{B}_0 and \mathbf{q} are both parallel to the c axis of the crystal (Faraday configuration), one should see a peak splitting due to valley polarization in the contribution from the W2 nodes to the Kerr angle. No such splitting would be present in the contribution from the W1 nodes, because these are not tilted along the c axis [27]. The experimental distinction of the contributions from W1 and W2 nodes to the valley polarization is made possible by

their clearly different optical gaps (≈ 25 meV in the case of W1 nodes, and ≈ 4 meV in the case of W2 nodes). On the other hand, if \mathbf{B}_0 is along the c axis of the crystal but \mathbf{q} is along the a or b axis (Voigt configuration), a peak in the Kerr angle will emulate the blueshift of the plasmon frequency as a function of B_0 . Both W1 and W2 nodes contribute to this blueshift.

The analysis becomes more complicated at weaker magnetic fields, where quantum limit is attained for the W2 nodes but not for the W1 nodes. In this regime, interband transitions between nonchiral Landau levels of the W1 nodes will result in additional low-frequency features in the absorption spectrum and in the Kerr angle, which could make it more difficult to resolve the valley polarization signal coming from the W2 nodes. Also, the contribution from the nonchiral Landau levels of the W1 nodes to the plasmon frequency will not in general scale as \sqrt{B} (depending on the distance in energy between the Fermi level and the bottom of each nonchiral Landau level). At the same time, the chiral Landau levels of both W1 and W2 nodes will still make a contribution to ω_p that scales as \sqrt{B} .

In our theory we have neglected nonlinear terms that are present in the energy dispersion of real WSMs at zero magnetic field. The impact of those terms in our main results, unimportant if the Fermi level is close to the Weyl nodes, is twofold. First, nonlinear terms in the energy dispersion give rise to a valley polarization, much like the tilt of the Weyl cones does [12]. As such, nonlinear terms produce features in the Kerr angle that are associated with the valley polarization, even in the absence of a tilt. Second, nonlinear terms in the energy dispersion can change the magnetic field dependence of the plasmon frequency. For example, if the chemical potential is near the bottom of the band that connects two chiral Landau levels in a real WSM, then a calculation that assumes a parabolic dispersion gives a plasmon frequency that is independent of the magnetic field. When the chemical potential increases and reaches the linear regime of the electronic dispersion, the plasmon frequency becomes a function of the magnetic field as in our model of the WSM. The latter is the regime of interest for us.

In real WSMs, the Fermi velocity near a Weyl node is anisotropic. Yet, this anisotropy can be incorporated in our isotropic model by an appropriate scaling of variables: $v_x(p_x + eA_x)\sigma_x + v_y(p_y + eA_y)\sigma_y + v_z(p_z + eA_z)\sigma_z + v_F \mathbf{t} \cdot \mathbf{p} = v_F(\tilde{p}_x + e\tilde{A}_x)\sigma_x + v_F(\tilde{p}_y + e\tilde{A}_y)\sigma_y + v_F(\tilde{p}_z + e\tilde{A}_z)\sigma_z + v_F \tilde{\mathbf{t}} \cdot \tilde{\mathbf{p}}$, where $v_i = v_F \alpha_i$ (for $i = x, y, z$) are the anisotropic Fermi velocities, $\tilde{p}_i = \alpha_i p_i$ are the rescaled momenta, $\tilde{t}_i = t_i / \alpha_i$ is the rescaled tilt, and $\tilde{A}_i = \alpha_i A_i$ is the rescaled vector potential. Independently rescaling the Hamiltonians for each node, all steps of our calculation can be essentially repeated. Based on this, we expect that the valley polarization and the blueshift of the plasmon frequency are robust to Fermi velocity anisotropies, at least qualitatively. A precise quantitative study is beyond the scope of the present work.

Finally, real WSMs host Fermi arc surface states. The contribution from those Fermi arcs to the magneto-optical response, neglected in our theory, should not significantly affect our main predictions, as the penetration depth of the electromagnetic waves in weakly doped bulk WSMs can largely

exceed the localization length of the surface states at the Fermi level.

ACKNOWLEDGMENTS

R.C. and I.G. were supported by grants from the Natural Sciences and Engineering Research Council of Canada (NSERC). J.-M.P. was supported by scholarships from NSERC and Fonds de Recherche du Québec - Nature et Technologies (FRQNT). Computer time was provided by Calcul Québec and Compute Canada. The authors thank S. Bertrand for helpful discussions.

APPENDIX A: EIGENSTATES OF TILTED WEYL CONES

A transverse static magnetic field $\mathbf{B} = B_0 \hat{\mathbf{z}}$ is added via the Peierls substitution $\mathbf{p} \rightarrow \mathbf{P} = \mathbf{p} + e\mathbf{A}$, with the vector potential $\mathbf{A} = (0, Bx, 0)$ ($e > 0$ for an electron) taken in the Landau gauge. The Hamiltonian $h_1(\mathbf{p})$ for node 1 becomes

$$h_1(\mathbf{P}) = h_1^{(0)}(\mathbf{P}) + W_1(\mathbf{P}), \quad (\text{A1})$$

with

$$h_1^{(0)}(\mathbf{P}) = v_F \begin{pmatrix} P_z & P_x - iP_y \\ P_x + iP_y & -P_z \end{pmatrix}, \quad (\text{A2})$$

the Hamiltonian in the absence of a tilt, and with

$$W_1(\mathbf{P}) = v_F \begin{pmatrix} \mathbf{t} \cdot \mathbf{P} & 0 \\ 0 & \mathbf{t} \cdot \mathbf{P} \end{pmatrix}, \quad (\text{A3})$$

the perturbation due to the tilt.

The Hamiltonian $h_1^{(0)}(\mathbf{p})$ is easily diagonalized by defining the ladder operators

$$a = \frac{\ell}{\sqrt{2}\hbar} (P_x - iP_y), \quad (\text{A4})$$

$$a^\dagger = \frac{\ell}{\sqrt{2}\hbar} (P_x + iP_y). \quad (\text{A5})$$

The energy spectrum of $h_1^{(0)}(\mathbf{p})$ consists of both positive and negative energy Landau levels. We classify them with the indices n, s where $n = 0, 1, 2, 3, \dots$ is always positive and $s = +1 (-1)$ is a band index for the positive (negative) energy levels. For node 1:

$$E_{1,0}(p_z) = -v_F p_z, \quad (\text{A6})$$

$$E_{1,n \neq 0,s}(p_z) = sv_F \sqrt{2 \frac{\hbar^2}{\ell^2} n + p_z^2}, \quad (\text{A7})$$

with the corresponding eigenstates

$$w_{1,n,s,X}(p_z, \mathbf{r}) = \frac{1}{\sqrt{L_z}} \begin{pmatrix} u_{1,n,s}(p_z) h_{n-1,X}(x, y) \\ v_{1,n,s}(p_z) h_{n,X}(x, y) \end{pmatrix} e^{ip_z z/\hbar}. \quad (\text{A8})$$

In these equations, $\ell = \sqrt{\hbar/eB}$ is the magnetic length and the wave functions $h_{n,X}(x, y)$ are the eigenstates of a two-dimensional electron gas in a transverse magnetic field in the Landau gauge:

$$h_{n,X}(x, y) = \frac{1}{\sqrt{L_y}} \varphi_n(x - X) e^{-iXy/\ell^2}, \quad (\text{A9})$$

with $\varphi_n(x)$ the eigenstates of the one-dimensional harmonic oscillator and n and X the Landau level and guiding-center indices respectively.

The coefficients $u_{1,n,s,p_z}, v_{1,n,s,p_z}$, which are independent of X , are given for $n \neq 0$ by

$$\begin{pmatrix} u_{1,n,s}(p_z) \\ v_{1,n,s}(p_z) \end{pmatrix} = \frac{1}{\sqrt{2}} \begin{pmatrix} -is \sqrt{1 - \frac{v_F p_z}{E_{1,n,s}(p_z)}} \\ \sqrt{1 + \frac{v_F p_z}{E_{1,n,s}(p_z)}} \end{pmatrix}, \quad (\text{A10})$$

and obey the normalization condition $|u_{1,n,s}(p_z)|^2 + |v_{1,n,s}(p_z)|^2 = 1$. For the chiral Landau level $n = 0$, the eigenstate is simply

$$\begin{pmatrix} u_{1,0}(p_z) \\ v_{1,0}(p_z) \end{pmatrix} = \begin{pmatrix} 0 \\ 1 \end{pmatrix} \quad (\text{A11})$$

and there is no band index in this case. The eigenenergies are independent of X so that each level (n, s, p_z) has a degeneracy given by $N_\varphi = S/2\pi\ell^2$ with $S = L_x L_y$ the area of the electron gas in the x - y plane (L_z is its extension in the z direction).

We must now obtain the energies and eigenvectors for tilted cones. Although an analytical solution exists [9], it is more convenient to use a numerical approach to the eigenvalue problem since we can then study the system for arbitrary orientations of the magnetic field and tilt vector or consider more complex Hamiltonians with, for example, nonlinear terms in the energy spectrum [13].

We write the many-body Hamiltonian for the four-node model as

$$\mathcal{H} = \sum_{\tau} \int d^3 r \psi_{\tau}^{\dagger}(\mathbf{r}) h_{\tau}(\mathbf{r}) \psi_{\tau}(\mathbf{r}) \quad (\text{A12})$$

and expand the fermionic field operators $\psi_{\tau}(\mathbf{r})$ onto the $\{w_{\tau,n,s,X}(p_z, \mathbf{r})\}$ basis (we leave as implicit the fact that \mathbf{t} depends on the node index τ)

$$\psi_{\tau}(\mathbf{r}) = \sum_{n,X,p_z} w_{\tau,n,s,X}(p_z, \mathbf{r}) c_{\tau,n,s,X,p_z}, \quad (\text{A13})$$

where c_{τ,n,s,X,p_z} is the annihilation operator for an electron in the $w_{\tau,n,s,X,p_z}(\mathbf{r})$ state. The many-body Hamiltonian can be written as

$$\begin{aligned} \mathcal{H} = & \sum_{\tau,n,s,p_z} [E_{\tau,n,s}(p_z) + v_F t_z p_z] c_{\tau,n,s,X,p_z}^{\dagger} c_{\tau,n,s,X,p_z} \\ & + \frac{\hbar v_F}{\sqrt{2}\ell} \sum_{\tau,n,n',s,s',p_z} W_{\tau,n,s,n',s'}(p_z) c_{\tau,n,s,X,p_z}^{\dagger} c_{\tau,n',s',X,p_z}. \end{aligned} \quad (\text{A14})$$

The matrix elements $W_{\tau,n,s,n',s'}(p_z)$ are defined by

$$\begin{aligned} W_{\tau,n,s,n',s'}(p_z) = & \int d^3 r w_{\tau,n,s,n',s'}^{\dagger}(p_z, \mathbf{r}) \\ & \times (t_- a^{\dagger} + t_+ a) w_{\tau,n',s',X}(p_z, \mathbf{r}), \end{aligned} \quad (\text{A15})$$

with the definition

$$t_{\pm} = t_x \pm it_y. \quad (\text{A16})$$

Their calculation gives

$$\begin{aligned} W_{\tau,n,s,n',s'}(p_z) = & -it_+ u_{\tau,n,s}^*(p_z) u_{\tau,n+1,s'}(p_z) \sqrt{n} \delta_{n',n+1} \\ & -it_+ v_{\tau,n,s}^*(p_z) v_{\tau,n+1,s'}(p_z) \sqrt{n+1} \delta_{n',n+1} \end{aligned}$$

$$\begin{aligned}
& +it_-u_{\tau,n,s}^*(p_z)u_{\tau,n-1,s'}(p_z)\sqrt{n-1}\delta_{n',n-1} \\
& +it_-v_{\tau,n,s}^*(p_z)v_{\tau,n-1,s'}(p_z)\sqrt{n}\delta_{n',n-1}.
\end{aligned} \quad (\text{A17})$$

The linear dispersion being valid only in a small region around each Weyl node, an appropriate high-energy cutoff must be applied to the summation over p_z . That cutoff is assumed to be small compared to the internodal separation in momentum space.

We define the superindices $I = n, s$ and $J = n', s'$ in order to write the Hamiltonian \mathcal{H} in the matrix form:

$$\mathcal{H} = \sum_{\tau, X, p_z} \sum_{I, J} c_I^\dagger(\tau, X, p_z) F_{I, J}(\tau, p_z) c_J(\tau, X, p_z), \quad (\text{A18})$$

where $c_J(\tau, X, p_z)$ stands for the vector $(c_{\tau,1,X,p_z}, c_{\tau,2,X,p_z}, c_{\tau,3,X,p_z}, \dots, c_{\tau,N,X,p_z})$, where N is the number of Landau levels n, s kept in the calculation and $F_{I, J}(\tau, p_z)$ is the $N \times N$ matrix given by

$$F_{I, J}(\tau, p_z) = [E_{\tau, I}(p_z) + v_F t_z p_z] \delta_{I, J} + W_{\tau, I, J}(p_z), \quad (\text{A19})$$

which is independent of the guiding-center index X .

The matrix \mathbf{F} is Hermitian and so can be diagonalized by a unitary transformation

$$\mathbf{F} = \mathbf{U} \mathbf{D} \mathbf{U}^\dagger, \quad (\text{A20})$$

where \mathbf{U} is the matrix of the eigenvectors of F and D the diagonal matrix of its eigenvalues $E_I(\tau, p_z)$, which are the energy of the Landau levels in the presence of the tilt.

Defining new operators $d_I(\tau, X, p_z)$ by

$$d_I(\tau, X, p_z) = \sum_J (U^\dagger)_{I, J} c_J(\tau, X, p_z), \quad (\text{A21})$$

we get the final result

$$\mathcal{H} = \sum_{\tau, X, p_z} \sum_I E_I(\tau, p_z) d_I^\dagger(\tau, X, p_z) d_I(\tau, X, p_z). \quad (\text{A22})$$

We also consider the case where the magnetic field is in the $\hat{\mathbf{x}}$ direction. The analysis proceeds in a similar way.

The analytical results [9] for the energy levels of the tilted cone $\tau = 1$ are

$$\begin{aligned}
E_{n=0, p_\parallel} &= v_F t_\parallel p_\parallel - \frac{v_F}{\gamma} p_\parallel, \\
E_{n \neq 0, p_\parallel} &= v_F t_\parallel p_\parallel + s \frac{1}{\gamma} \sqrt{v_F^2 p_\parallel^2 + \frac{2\hbar^2 n v_F^2}{\gamma \ell^2}},
\end{aligned} \quad (\text{A23})$$

where $p_\parallel = \mathbf{p} \cdot \hat{\mathbf{B}}$, $t_\parallel = \mathbf{t} \cdot \hat{\mathbf{B}}$, and $\gamma = (1 - |\mathbf{t} \times \hat{\mathbf{B}}|^2)^{-1/2}$.

APPENDIX B: CURRENT OPERATOR

The single-particle current operator for node τ is defined by

$$\mathbf{j}_\tau = - \left. \frac{\partial h_\tau(\mathbf{p})}{\partial \mathbf{A}_{\text{ext}}} \right|_{\mathbf{A}_{\text{ext}} \rightarrow 0} = -e v_F (\boldsymbol{\sigma} + \mathbf{t} \boldsymbol{\sigma}_0), \quad (\text{B1})$$

where \mathbf{A}_{ext} is the vector potential of an external electromagnetic field. The total many-body current for this node is given

by

$$\begin{aligned}
\mathbf{J}_\tau &= \int d^3 r \psi_\tau^\dagger(\mathbf{r}) \mathbf{j}_\tau \psi_\tau(\mathbf{r}) \\
&= -e v_F \sum_{\tau, p_z, X} \sum_{I, J} \mathbf{\Lambda}_{I, J}(\tau, p_z) c_{\tau, I, X, p_z}^\dagger c_{\tau, J, X, p_z} \\
&= -e v_F \sum_{\tau, p_z, X} \sum_{I, J} \mathbf{\Upsilon}_{I, J}(\tau, p_z) d_I^\dagger(\tau, X, p_z) d_J(\tau, X, p_z),
\end{aligned} \quad (\text{B2})$$

with the matrix elements defined by

$$\mathbf{\Lambda}_{I, J}(\tau, p_z) = \int d^3 r w_{\tau, I, X, p_z}^\dagger(\mathbf{r}) (\boldsymbol{\sigma} + \mathbf{t} \boldsymbol{\sigma}_0) w_{\tau, J, X, p_z}(\mathbf{r}) \quad (\text{B3})$$

and the definition

$$\mathbf{\Upsilon} = \mathbf{U}^\dagger \mathbf{\Lambda} \mathbf{U}. \quad (\text{B4})$$

The matrix elements

$$\begin{aligned}
\mathbf{\Lambda}_{n, s, n', s'} &= u_{\tau, n, s}^*(p_z) v_{\tau, n-1, s'}(p_z) \delta_{n', n-1} (\hat{\mathbf{x}} - i \hat{\mathbf{y}}) \\
&+ v_{\tau, n, s}^*(p_z) u_{\tau, n+1, s'}(p_z) \delta_{n', n+1} (\hat{\mathbf{x}} + i \hat{\mathbf{y}}) \\
&+ u_{\tau, n, s}^*(p_z) u_{\tau, n, s'}(p_z) \delta_{n', n} \hat{\mathbf{z}} \\
&- v_{\tau, n, s}^*(p_z) v_{\tau, n, s'}(p_z) \delta_{n', n} \hat{\mathbf{z}} + \mathbf{t} \delta_{n, n'} \delta_{s, s'}.
\end{aligned} \quad (\text{B5})$$

APPENDIX C: MOKE IN A NORMAL METAL

For comparison with the Kerr rotation in a WSM, we give a short review of the Kerr effect in a normal three-dimensional metal in a transverse magnetic field. We consider a system in which the half-space $z < 0$ (region 1) is occupied by a non-conducting medium with relative dielectric constant $\varepsilon_1 = 1$ and the half-space $z > 0$ (region 2) is occupied by the normal metal. We use the results of Sec. IV, but with the relative dielectric tensor $\overleftrightarrow{\varepsilon}$ of a normal metal.

1. Longitudinal propagation ($\mathbf{q} \parallel \mathbf{B}_0 \parallel \hat{\mathbf{z}}$)

For a magnetic field $\mathbf{B} = B_0 \hat{\mathbf{z}}$, the (relative) dielectric tensor for a normal metal in the Drude model has the same symmetry as $\overleftrightarrow{\varepsilon}$ in Eq. (40). The components are given by

$$\varepsilon_{xx} = \varepsilon_{yy} = 1 - \frac{\omega_p^2}{\omega} \frac{\omega + \frac{i}{\tau_m}}{\left(\omega + \frac{i}{\tau_m}\right)^2 - \omega_c^2}, \quad (\text{C1})$$

$$\varepsilon_{xy} = -\varepsilon_{yx} = \frac{\omega_p^2}{\omega} \frac{i \omega_c}{\left(\omega + \frac{i}{\tau_m}\right)^2 - \omega_c^2}, \quad (\text{C2})$$

$$\varepsilon_{zz} = 1 - \frac{\omega_p^2}{\omega} \frac{1}{\omega + \frac{i}{\tau_m}}, \quad (\text{C3})$$

where τ_m is the transport relaxation time, $\omega_c = e B_0 / m$ is the cyclotron frequency, and $\omega_p = \sqrt{ne^2 / \varepsilon_0 m}$, with ε_0 the free space permittivity and m the effective mass of the electrons. The dispersion relation of Eq. (42) for the two circularly polarized electromagnetic waves in a normal metal becomes

$$q_\pm(\omega) = \frac{\omega}{c} \sqrt{\varepsilon_\pm}, \quad (\text{C4})$$

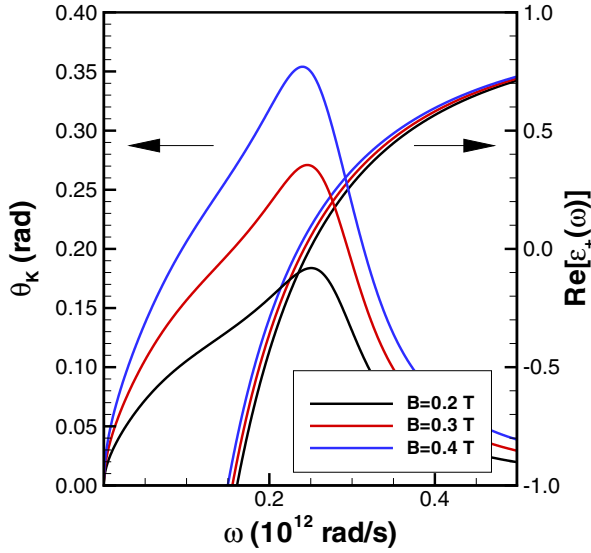


FIG. 9. Kerr angle in the Faraday configuration (left y axis) and dielectric function $\text{Re}[\varepsilon_+(\omega)]$ (right y axis) as a function of frequency for an external magnetic field $B_0 = 0.2, 0.3, 0.4$ and an electronic density $n_e = 0.25 \times 10^{20} \text{ m}^{-3}$.

with

$$\varepsilon_{\pm}(\omega) = \varepsilon_{xx} \mp i\varepsilon_{xy} = 1 - \frac{\omega_p^2}{\omega} \left(\frac{1}{\omega \pm \omega_c + \frac{i}{\tau_m}} \right). \quad (\text{C5})$$

In the pure limit ($\tau_m \rightarrow \infty$), the zeros of ε_{\pm} are given by (keeping only positive frequencies)

$$\omega_{\pm} = \frac{\mp \omega_c + \sqrt{\omega_c^2 + 4\omega_p^2}}{2}. \quad (\text{C6})$$

We remark that Eq. (C5) remains valid in the quantum case, when the kinetic energy is quantized into Landau levels.

For an incident wave linearly polarized at $\theta_l = \pi/4$ from the x axis with amplitude E_0^x , the reflection coefficients are given by Eqs. (45a) and (45b), the Kerr angle is obtained from Eq. (60) and the phases θ_R^x and θ_R^y are defined in Eq. (56).

Figure 9 shows the Kerr angle θ_K (left y axis) calculated from Eq. (58) (black line) for the same magnetic fields $B_0 = 0.2, 0.3, 0.4$ T used in Fig. 7 and the same electronic density (equivalent to the density of one node) $n_e = 0.25 \times 10^{20} \text{ m}^{-3}$. The relaxation time is taken to be $\tau_m = 10$ ps. As in a WSM, the big peak in the Kerr angle occurs near the zero of the dielectric function $\text{Re}[\varepsilon_+(\omega)]$ (right y axis), i.e., at ω_+ , and is shifted to lower frequencies with increasing magnetic field. There is no particular feature of the Kerr angle at the cyclotron frequency $\omega_c = eB_0/m$, which is $\omega_c = 0.035 \times 10^{12} \text{ rad/s}$ for $B = 0.2$ T. The density that we use in these calculations is much smaller than that in a normal metal. Our goal is to compare the predictions of the Drude model with that of the WSM, where our numerical calculation uses that particular density.

Figure 10 shows what happens if we increase the density to $n_e = 0.25 \times 10^{22} \text{ m}^{-3}$. There is more structure in the Kerr angle, but the maximum still occurs at $\text{Re}[\varepsilon_+(\omega_+)] = 0$, i.e., at a frequency 10 times bigger, and is again redshifted in frequency by an increasing magnetic field. The shoulder on

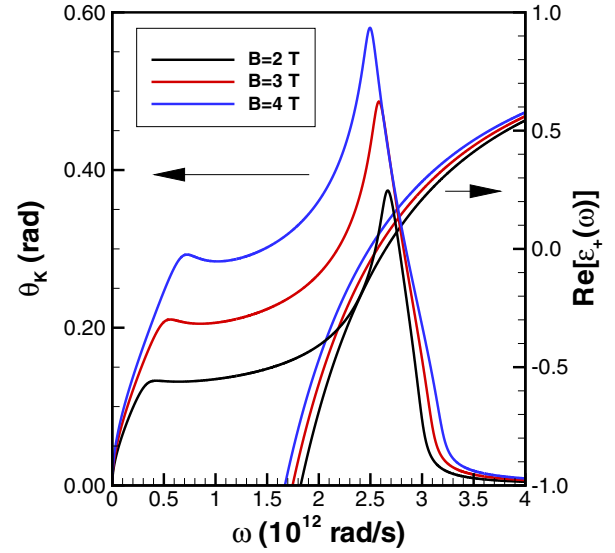


FIG. 10. Kerr angle in the Faraday configuration (left y axis) and dielectric function $\text{Re}[\varepsilon_+(\omega)]$ (right y axis) as a function of frequency for an external magnetic field $B_0 = 2, 3, 4$ and an electronic density $n_e = 0.25 \times 10^{22} \text{ m}^{-3}$.

the left occurs at the smallest of the two zeros of $\text{Re}[\varepsilon_-(\omega)]$. At a density of $n_e = 1 \times 10^{29} \text{ m}^{-3}$, typical of a real metal and keeping $\tau_m = 10$ ps with $B_0 = 10$ T, the Kerr angle is almost constant at $\theta_K = 0.1$ mrad. It peaks at $\text{Re}[\varepsilon_+(\omega_+)] = 0$, i.e., at $\omega_+ = 18.9 \times 10^{15} \text{ rad/s}$ where it reaches 3.5 mrad. The frequency ω_+ is then given by Eq. (C6), with $\omega_c \tau_m \ll \omega_p \tau_m$ and $\omega_+ = \omega_p$. The Kerr angle decreases with decreasing value of τ_m .

2. Transverse propagation ($\mathbf{q} \perp \mathbf{B}_0 \parallel \hat{\mathbf{x}}$)

With $\mathbf{B} = B_0 \hat{\mathbf{x}}$, the dielectric tensor for a normal metal has the symmetry of $\overleftrightarrow{\varepsilon}$ in Eq. (49), except that $\varepsilon_{yy} = \varepsilon_{zz}$ and

$$\varepsilon_{xx} = 1 - \frac{\omega_p^2}{\omega} \frac{1}{\left(\omega + \frac{i}{\tau_m}\right)}, \quad (\text{C7})$$

$$\varepsilon_{yy} = \varepsilon_{zz} = 1 - \frac{\omega_p^2}{\omega} \frac{\omega + \frac{i}{\tau_m}}{\left(\omega + \frac{i}{\tau_m}\right)^2 - \omega_c^2}, \quad (\text{C8})$$

$$\varepsilon_{yz} = -\varepsilon_{zy} = -\frac{\omega_p^2}{\omega} \frac{i\omega_c}{\left(\omega + \frac{i}{\tau_m}\right)^2 - \omega_c^2}. \quad (\text{C9})$$

Maxwell equations for this Voigt configuration give two solutions with the polarization parallel or perpendicular to the magnetic field and dispersion

$$q_{\parallel} = \frac{\omega}{c} \sqrt{\varepsilon_{xx}}, \quad (\text{C10})$$

$$q_{\perp} = \frac{\omega}{c} \sqrt{\varepsilon_v}, \quad (\text{C11})$$

where the Voigt dielectric constant is defined by

$$\varepsilon_v = \varepsilon_{yy} + \frac{\varepsilon_{yz}^2}{\varepsilon_{zz}}. \quad (\text{C12})$$

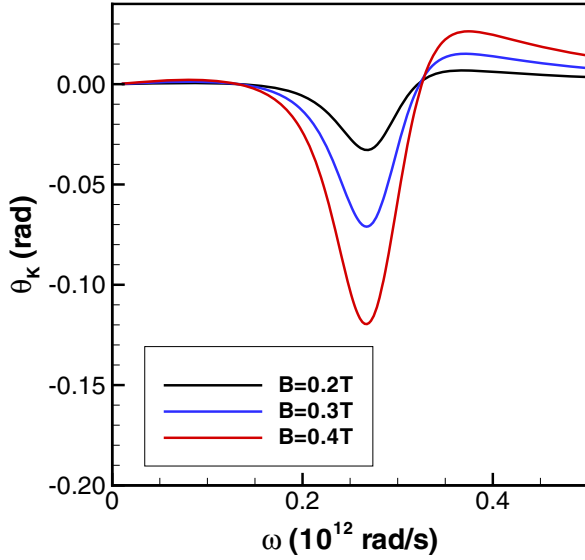


FIG. 11. Kerr angle θ_K in the Voigt configuration as a function of frequency for $B_0 = 0.2, 0.3, 0.4$ T. Parameters: $n_e = 0.25 \times 10^{20} \text{ m}^{-3}$ and $\tau_m = 10$ ps.

In this configuration there is an induced field in the direction of propagation, which is given by

$$E_z = -\frac{\varepsilon_{zy}}{\varepsilon_{zz}} E_y. \quad (\text{C13})$$

To see any variations of the Kerr angle, the incident wave has to be polarized at an angle with respect to the x and y axis. The reflected electric field components are then obtained from Eq. (55), while the Kerr angle is obtained from Eq. (61). In our calculation, we assume that the incident wave is linearly polarized at an angle $\theta_I = \pi/4$ with respect to the x axis, so that $E_0^x(\omega) = E_0^y(\omega)$. The dielectric function $\text{Re}[\varepsilon_{xx}(\omega)] = 0$ at $\omega = \omega_p = \sqrt{ne^2/m\varepsilon_0}$.

Figure 11 shows the Kerr angle θ_K in the Voigt configuration for three different values of the magnetic field, i.e., $B_0 = 0.2, 0.3, 0.4$ T, the same values as in Fig. 7 for the WSM. The carrier density is $n_e = 0.25 \times 10^{20} \text{ m}^{-3}$ and the relaxation time is $\tau_m = 10$ ps. The Kerr angle is an order of magnitude smaller than in the Faraday configuration. Its minimum occurs near the plasmon frequency while, in a WSM (see Fig. 7), it is the maximum of the Kerr angle that occurs at that frequency. Because the plasmon frequency is independent of B_0 in a metal, the frequency at which the minimum in θ_K occurs is also independent of B_0 . The minimum in θ_K increases negatively with B_0 . We find numerically that the frequency at which the Kerr angle is maximal $\theta_{K,\text{max}} \propto B_0^2$ while $\theta_{K,\text{max}} \propto \sqrt{B_0}$ in a WSM. In contrast with a WSM, this maximum does not seem to be associated with any feature in ε_v or ε_{xx} .

APPENDIX D: MAGNETIC-FIELD DEPENDENCE OF THE PEAK IN $\varepsilon_+(\omega)$

In this Appendix we derive the magnetic-field dependence of the low-energy peak in the Kerr angle shown in Figs. 5 and 6. This peak occurs at a frequency ω_f given by the condi-

tion $\text{Re}[\varepsilon_+(\omega_f)] = 0$, i.e., at

$$\varepsilon_0\omega_f = \sigma''_{xx} - \sigma'_{xy} \quad (\text{D1})$$

for a magnetic field pointing in the z direction. To simplify the calculation we assume zero tilt. In this case, only σ_{zz} is nonzero for the intraband transitions and they then do not contribute to ω_f . In terms of the current response function, Eq. (D1) becomes

$$\varepsilon_0\omega_f^2 = \chi'_{xx}(\omega_f) - \chi'_{xx}(0) + \chi''_{xy}(\omega_f). \quad (\text{D2})$$

We assume that the main contributions to χ_{ij} come from the transition $n = -1$ to $n = 0$ and $n = 0$ to $n = 1$. For these transitions and for node 1

$$E_1(p) - E_0(p) = \frac{\hbar v_F}{\ell} p\ell + \frac{\hbar v_F}{\ell} \sqrt{2 + p^2\ell^2} \quad (\text{D3})$$

and

$$E_0(p) - E_{-1}(p) = -\frac{\hbar v_F}{\ell} p\ell + \frac{\hbar v_F}{\ell} \sqrt{2 + p^2\ell^2}. \quad (\text{D4})$$

The matrix elements of the current operator in χ_{ij} are given by

$$\Upsilon_{01}^{(x)}(p)\Upsilon_{10}^{(x)}(p) = \frac{1}{1 + \frac{1}{2}(p\ell - \sqrt{2 + p^2\ell^2})^2}, \quad (\text{D5})$$

with the relation

$$\Upsilon_{-1,0}^{(x)}(p)\Upsilon_{0,-1}^{(y)}(p) = i\Upsilon_{0,1}^{(x)}(-p)\Upsilon_{1,0}^{(x)}(-p). \quad (\text{D6})$$

Since $\hbar\omega_f \ll E_1(p) - E_0(p)$, $E_0(p) - E_{-1}(p)$, we can expand the denominator in the current response to get

$$\chi'_{xx}(\omega_f) - \chi'_{xx}(0) = (\alpha_{0,1} + \alpha_{-1,0})\omega_f^2, \quad (\text{D7})$$

$$\chi''_{xy}(\omega_f) = (\beta_{0,1} + \beta_{-1,0})\omega_f. \quad (\text{D8})$$

The frequency

$$\omega_f = \frac{\beta_{0,1} + \beta_{-1,0}}{\varepsilon_0 - (\alpha_{0,1} + \alpha_{-1,0})}. \quad (\text{D9})$$

The coefficients in Eq. (D9) are given by

$$\begin{aligned} \beta_{1,0} &= \frac{2e^2}{4\pi^2\hbar\ell} \int_{-\infty}^{+\infty} dy \Upsilon_{0,1}^{(x)}(y)\Upsilon_{1,0}^{(x)}(y) \frac{f_1(y) - f_0(y)}{[\overline{E}_1(y) - \overline{E}_0(y)]^2} \\ &= \frac{e^2}{4\pi^2\hbar\ell} \int_{-\infty}^{p_F\ell} dy \frac{1}{y^2 - y\sqrt{y^2 + 2} + 2} \end{aligned} \quad (\text{D10})$$

and

$$\begin{aligned} \beta_{0,-1} &= \frac{2e^2}{4\pi^2\hbar\ell} \int_{-\infty}^{+\infty} dy \Upsilon_{-1,0}^{(x)}(y)\Upsilon_{0,-1}^{(x)}(y) \frac{f_0(y) - f_{-1}(y)}{[\overline{E}_0(y) - \overline{E}_{-1}(y)]^2} \\ &= -\frac{e^2}{4\pi^2\hbar\ell} \int_{-\infty}^{-p_F\ell} dy \frac{1}{y^2 - y\sqrt{y^2 + 2} + 2}. \end{aligned} \quad (\text{D11})$$

They combine to give

$$\beta_{1,0} + \beta_{0,-1} = \frac{e^2 p_F}{4\pi^2\hbar}, \quad (\text{D12})$$

where p_F is the Fermi momentum and $\overline{E}_n(y)$ are the single-particle energies expressed in units of $\hbar v_F/\ell$.

For the coefficients α , the definitions are

$$\begin{aligned}\alpha_{1,0} &= \frac{2e^2}{4\pi^2\hbar v_F} \int_{-\infty}^{+\infty} dy \Upsilon_{0,1}^{(x)}(y) \Upsilon_{1,0}^{(x)}(y) \frac{f_1(y) - f_0(y)}{[\bar{E}_1(y) - \bar{E}_0(y)]^3} \\ &= -\frac{2e^2}{4\pi^2\hbar v_F} \int_{-\infty}^{p_F\ell} dy \frac{1}{1 + \frac{1}{2}(y + \sqrt{2 + y^2})^2} \\ &\quad \times \frac{1}{(-y + \sqrt{2 + y^2})^3}\end{aligned}\quad (\text{D13})$$

and

$$\begin{aligned}\alpha_{0,-1} &= \frac{2e^2}{4\pi^2\hbar v_F} \int_{-\infty}^{+\infty} dy \Upsilon_{0,-1}^{(x)}(y) \Upsilon_{-1,0}^{(x)}(y) \frac{f_{-1}(y) - f_0(y)}{[\bar{E}_{-1}(y) - \bar{E}_0(y)]^3} \\ &= \frac{2e^2}{4\pi^2\hbar v_F} \int_{-\infty}^{-p_F\ell} dy \frac{1}{1 + \frac{1}{2}(y + \sqrt{2 + y^2})^2} \\ &\quad \times \frac{1}{(y - \sqrt{2 + y^2})^3}.\end{aligned}\quad (\text{D14})$$

They combine to give

$$\alpha_{1,0} + \alpha_{0,-1} = -\frac{e^2}{8\pi^2\hbar v_F} (p_F\ell + \sqrt{2 + (p_F\ell)^2}). \quad (\text{D15})$$

Within the small-frequency approximation, the expression for the frequency ω_f is now, summing the contribution of the four nodes:

$$\omega_f = \frac{\frac{4e^2 p_F}{4\pi^2\hbar\epsilon_0}}{\left[1 + \frac{4e^2}{8\pi^2\hbar v_F\epsilon_0} (p_F\ell + \sqrt{2 + (p_F\ell)^2})\right]}. \quad (\text{D16})$$

The density of states for the chiral level of one node is $g_{n=0}(E) = \frac{1}{4\pi^2\ell^2\hbar v_F}$, so that the Fermi momentum is given by $n_e = g_{n=0}(E)\hbar v_F p_F$, where n_e is the density in node 1. Thus $p_F\ell = 4\pi^2\ell^3 n_e$. With $n_e = 0.25 \times 10^{20} \text{ m}^{-3}$ and $B_0 = 0.2 \text{ T}$, i.e., $p_F\ell = 0.19 \ll 2$ and we can further approximate

$$\omega_f = \frac{1}{\left(1 + 4\frac{1}{\sqrt{2\pi}}\alpha_g\right)} \frac{4en_e}{\epsilon_0 B_0}, \quad (\text{D17})$$

where $\alpha_g = e^2/4\pi\hbar\epsilon_0 v_F$ is the effective fine-structure constant for the WSM. The frequency shift of the large peak in the Faraday configuration is thus inversely proportional to the magnetic field. We have checked that Eq. (D16) is in good agreement with the numerical value of $\text{Re}[\epsilon_+(\omega_f)] = 0$. As an example, for $B_0 = 0.2 \text{ T}$, we find $\omega_f \approx 1.06 \times 10^{12} \text{ rad/s}$ from Eq. (D16) which is indeed close to the numerical value $0.98 \times 10^{12} \text{ rad/s}$.

-
- [1] For a review of Weyl semimetals, see for example: P. Hosur and X.-L. Qi, *C. R. Phys.* **14**, 857 (2013); N. P. Armitage, E. J. Mele, and A. Vishwanath, *Rev. Mod. Phys.* **90**, 015001 (2018).
- [2] H. B. Nielsen and M. Ninomiya, *Phys. Lett. B* **105**, 219 (1981).
- [3] K. Y. Yang, Y. M. Lu, and Y. Ran, *Phys. Rev. B* **84**, 075129 (2011); G. Xu, H. Weng, Z. Wang, X. Dai, and Z. Fang, *Phys. Rev. Lett.* **107**, 186806 (2011); P. Goswami and S. Tewari, *Phys. Rev. B* **88**, 245107 (2013); A. A. Burkov and L. Balents, *Phys. Rev. Lett.* **107**, 127205 (2011); A. A. Zyuzin, S. Wu, and A. A. Burkov, *Phys. Rev. B* **85**, 165110 (2012).
- [4] J. H. Zhou, H. Jiang, Q. Niu, and J. R. Shi, *Chin. Phys. Lett.* **30**, 027101 (2013); Y. Chen, S. Wu, and A. A. Burkov, *Phys. Rev. B* **88**, 125105 (2013).
- [5] X. Wan, A. M. Turner, A. Vishwanath, and S. Y. Savrasov, *Phys. Rev. B* **83**, 205101 (2011); P. Hosur, *ibid.* **86**, 195102 (2012).
- [6] D. T. Son and B. Z. Spivak, *Phys. Rev. B* **88**, 104412 (2013); F. Wilczek, *Phys. Rev. Lett.* **58**, 1799 (1987); A. A. Zyuzin and A. A. Burkov, *Phys. Rev. B* **86**, 115133 (2012).
- [7] J. M. Shao and G. W. Yang, *AIP Adv.* **6**, 025312 (2016); Y. Jiang, Z. Dun, S. Moon, H. Zhou, M. Koshino, D. Smirnov, and Z. Jiang, *Nano Lett.* **18**, 7726 (2018); X. Yuan, Z. Yan, C. Song, M. Zhang, Z. Li, C. Zhang, Y. Liu, W. Wang, M. Zhao, Z. Lin, T. Xie, J. Ludwig, Y. Jiang, X. Zhang, C. Shang, Z. Ye, J. Wang, F. Chen, Z. Xia, D. Smirnov, X. Chen, Z. Wang, H. Yan, and F. Xiu, *Nat. Commun.* **9**, 1854 (2018).
- [8] P. E. C. Ashby and J. P. Carbotte, *Phys. Rev. B* **89**, 245121 (2014); C. J. Tabert, J. P. Carbotte, and E. J. Nicol, *ibid.* **93**, 085426 (2016); **94**, 039901(E) (2016).
- [9] S. Tchoumakov, M. Civelli, and M. O. Goerbig, *Phys. Rev. Lett.* **117**, 086402 (2016).
- [10] I. Crassee, J. Levallois, A. L. Walter, M. Ostler, A. Bostwick, E. Rotenberg, T. Seyller, D. van der Marel, and A. B. Kuzmenko, *Nat. Phys.* **7**, 48 (2011).
- [11] M. Kargarian, M. Randeria, and N. Trivedi, *Sci. Rep.* **5**, 12683 (2015).
- [12] S. Bertrand, J.-M. Parent, R. Côté, and I. Garate, *Phys. Rev. B* **100**, 075107 (2019).
- [13] S. Bertrand, I. Garate, and R. Côté, *Phys. Rev. B* **96**, 075126 (2017).
- [14] K. Sonowal, A. Singh, and A. Agarwal, *Phys. Rev. B* **100**, 085436 (2019).
- [15] J. Yang, J. Kim, and K.-S. Kim, *Phys. Rev. B* **98**, 075203 (2018).
- [16] A. L. Levy, A. B. Sushkov, F. Liu, B. Shen, N. Ni, H. D. Drew, and G. S. Jenkins, *Phys. Rev. B* **101**, 125102 (2020).
- [17] B. Cheng, T. Schumann, S. Stemmer, and N. P. Armitage, [arXiv:1910.13655](https://arxiv.org/abs/1910.13655).
- [18] P. E. C. Ashby and J. P. Carbotte, *Phys. Rev. B* **87**, 245131 (2013).
- [19] S. P. Mukherjee and J. P. Carbotte, *Phys. Rev. B* **96**, 085114 (2017).
- [20] B. J. Ramshaw, K. A. Modic, A. Shekhter, Y. Zhang, E.-A. Kim, P. J. W. Moll, M. D. Bachmann, M. K. Chan, J. B. Betts, F. Balakirev, A. Migliori, N. J. Ghimire, E. D. Bauer, F. Ronning, and R. D. McDonald, *Nat. Commun.* **9**, 2217 (2018).
- [21] P. Goswami, J. H. Pixley, and S. Das Sarma, *Phys. Rev. B* **92**, 075205 (2015).
- [22] H.-Z. Lu, S.-B. Zhang, and S. Q. Shen, *Phys. Rev. B* **92**, 045203 (2015).
- [23] S. Das Sarma and E. H. Hwang, *Phys. Rev. Lett.* **102**, 206412 (2009).
- [24] M. Balkanski and R. F. Wallis, *Many-Body Aspects of Solid State Spectroscopy* (North-Holland, Amsterdam, 1986).
- [25] C.-C. Lee, S.-Y. Xu, S.-M. Huang, D. S. Sanchez, I. Belopolski, G. Chang, G. Bian, N. Alidoust, H. Zheng, M. Neupane, B. Wang, A. Bansil, M. Z. Hasan, and H. Lin, *Phys. Rev. B* **92**, 235104 (2015).

- [26] D. Grassano, O. Pulci, A. M. Conte, and F. Bechstedt, [Sci. Rep.](#) **8**, 3534 (2018).
- [27] This is due to symmetry reasons. In the case of W1 nodes, located in the $k_z = 0$ plane of the Brillouin zone, any two time-reversed partner nodes are also related by the product of two mirror operations. Time-reversal enforces that t_z should have

the opposite sign at time-reversed partner nodes, whereas the product of the two mirrors imposes that t_z should be the same at the two nodes. Hence, t_z must be zero. No such constraint is present for W2 nodes, located at $k_z \neq 0$ planes of the Brillouin zone, because in this case time reversal does not connect two nodes at the same constant k_z plane.